



## RESEARCH ARTICLE

# Extracellular vesicle biogenesis of three-dimensional human pluripotent stem cells in a novel Vertical-Wheel bioreactor

Laureana Muok<sup>1</sup> | Li Sun<sup>1,2</sup>  | Colin Esmonde<sup>1</sup> | Hannah Worden<sup>3</sup> | Cynthia Vied<sup>2</sup> |  
 Leanne Duke<sup>2</sup> | Shaoyang Ma<sup>1</sup> | Olivia Zeng<sup>1</sup> | Tristan Driscoll<sup>1</sup> | Sunghoon Jung<sup>3</sup> |  
 Yan Li<sup>1</sup> 

<sup>1</sup>Department of Chemical and Biomedical Engineering, FAMU-FSU College of Engineering, Florida State University, Tallahassee, Florida, USA

<sup>2</sup>Department of Biomedical Sciences, College of Medicine, Florida State University, Tallahassee, Florida, USA

<sup>3</sup>PBS Biotech Inc, Camarillo, California, USA

## Correspondence

Yan Li, FAMU-FSU College of Engineering, Florida State University, 2525 Pottsdamer St., Tallahassee, FL 32310, USA. Email: yli4@fsu.edu

## Funding information

National Institutes of Health, Grant/Award Number: R01NS125016; National Science Foundation, Grant/Award Number: CBET-1652992; National Science Foundation, Grant/Award Number: CBET-1917618; National Science Foundation, Grant/Award Number: 2017869

## Abstract

Extracellular vesicles (EVs) secreted by human-induced pluripotent stem cells (hiPSCs) have great potential as cell-free therapies in various diseases, including prevention of blood–brain barrier senescence and stroke. However, there are still challenges in pre-clinical and clinical use of hiPSC-EVs due to the need for large-scale production of a large quantity. Vertical-Wheel bioreactors (VWBRs) have design features that allow the biomanufacturing of hiPSC-EVs using a scalable aggregate or microcarrier-based culture system under low shear stress. EV secretion by undifferentiated hiPSCs expanded as 3-D aggregates and on Synthemax II microcarriers in VWBRs were investigated. Additionally, two types of EV collection media, mTeSR and HBM, were compared. The hiPSCs were characterized by metabolite and transcriptome analysis as well as EV biogenesis markers. Protein and microRNA cargo were analysed by proteomics and microRNA-seq, respectively. The *in vitro* functional assays of microglia stimulation and proliferation were conducted. HiPSCs expanded as 3-D aggregates and on microcarriers had comparable cell number, while microcarrier culture had higher glucose consumption, higher glycolysis and lower autophagy gene expression based on mRNA-seq. The microcarrier cultures had at least 17–23 fold higher EV secretion, and EV collection in mTeSR had 2.7–3.7 fold higher yield than HBM medium. Microcarrier culture with mTeSR EV collection had a smaller EV size than other groups, and the cargo was enriched with proteins (proteomics) and miRNAs (microRNA-seq) reducing apoptosis and promoting cell proliferation (e.g. Wnt-related pathways). hiPSC-EVs demonstrated the ability of stimulating proliferation and M2 polarization of microglia *in vitro*. HiPSC expansion on microcarriers produces much higher yields of EVs than hiPSC aggregates in VWBRs. EV collection in mTeSR increases yield compared to HBM. The biomanufactured EVs from microcarrier culture in mTeSR have exosomal characteristics and are functional in microglia stimulation, which paves the ways for future *in vivo* anti-aging study.

## KEYWORDS

aggregates, extracellular vesicles, human pluripotent stem cells, microcarriers, multi-omics, Vertical-Wheel bioreactor

Laureana Muok and Li Sun contributed equally to this work.

This is an open access article under the terms of the [Creative Commons Attribution-NonCommercial License](https://creativecommons.org/licenses/by-nc/4.0/), which permits use, distribution and reproduction in any medium, provided the original work is properly cited and is not used for commercial purposes.

© 2024 Finnish Red Cross Blood Service. *Journal of Extracellular Biology* published by Wiley Periodicals LLC on behalf of International Society for Extracellular Vesicles.

## 1 | INTRODUCTION

Extracellular vesicles (EVs) are membrane-bound nanoparticles that are released by all types of cells (Zhou et al., 2021) and have been found in various bodily fluids, such as blood and urine. Exosomes are the subpopulation of EVs that have small size of 30–200 nm in diameter. Depending on cell source and microenvironment, EV cargo can consist of lipids, proteins and nucleic acids that can be delivered to the target cells (Dougherty et al., 2018). Studies have linked EVs to disease progression and cancer metastasis, which can use EVs to identify novel biomarkers as well as for cancer therapy (Liu & Su, 2019; Zhang et al., 2021). Human stem cell-derived EVs have therapeutic potential in treating various diseases such as cardiac injury (Adamiak et al., 2018; Liu et al., 2018), stroke and Alzheimer's disease (Cone et al., 2021; Zhang et al., 2019). Therefore, there has been an increased demand to examine the biological characteristics of EVs secreted by human pluripotent stem cells (hPSCs) including human-induced pluripotent stem cells (hiPSCs) and human embryonic stem cells, or hPSC-derived lineage-specific cells such as neural progenitors and mesenchymal stem cells (Jeske et al., 2020; Luo et al., 2021; Taheri et al., 2018).

hPSC-derived EVs have been shown to rejuvenate aged adult stem cells *in vitro*, rejuvenate senescent blood–brain barrier in ischaemic stroke *in vivo*, promote cardio-genesis and demonstrate immunomodulation and anti-inflammatory activities (Bi et al., 2022; Gong et al., 2020; Gu et al., 2022; Li et al., 2023; Liu et al., 2019; Louro et al., 2022; Upadhyaya et al., 2020; Xia et al., 2021). Several studies have indicated that EVs released by hiPSCs act as paracrine mediators influencing cell fate (Karnas et al., 2021). This is partially due to their ability to facilitate the transfer of genetic information and proteins from stem cells to injured host cells. An additional benefit that makes hPSC-EVs appealing for regenerative medicine is their ability to mimic stem cell properties and to cross blood–brain barrier (Upadhyaya et al., 2020). However, despite their potential, well-designed biomanufacturing systems are necessary to increase the consistency and scalability of hPSC-EV production.

Various culture parameters have been shown to promote EV secretion of human stem cells, including 3-D aggregate architecture, hypoxia, matrix stiffness and dynamic culture environment (Patel et al., 2018; Rocha et al., 2019; Yuan et al., 2022). Recently, shear stress in 3D microenvironment of bioreactors has been observed to enhance EV biogenesis and the EV cargo profiles (Debbi et al., 2022), which also has been shown in our previous studies using human mesenchymal stem cells (hMSCs) (Jeske et al., 2022, 2022, 2023). Vertical-Wheel bioreactors (VWBRs) have previously been used for the production of hMSCs on microcarriers (Lembong et al., 2020), hPSC aggregates, hPSCs on microcarriers (Borys et al., 2021; Cuesta-Gomez et al., 2023; Nogueira et al., 2021; Rodrigues et al., 2018; Vallabhaneni et al., 2023) and cerebellar spheroids (Silva et al., 2020, 2021). The unique design of the hydrodynamics in VWBRs results in 10-fold lower shear stress levels compared to traditional stirred tank bioreactors (0.1–0.3 dyn/cm<sup>2</sup> vs. 1–3 dyn/cm<sup>2</sup>, respectively) (Borys et al., 2021, 2020; Jeske et al., 2023, 2021). However, the use of VWBRs and the influence of different 3-D hPSC organization for hPSC-EV production has not been investigated to date.

Previously, our lab has investigated hMSC-EV production using Synthemax II microcarrier-based expansion in VWBRs (0.1 and 0.5 L) under agitation speeds of 25, 40 and 64 rpm (Jeske et al., 2023). The results showed a higher amount of EV secretion as well as upregulation of EV biogenesis markers and glycolysis genes for the bioreactor system when compared to static 2D culture. VWBRs may alter hMSC metabolic status (e.g. glycolysis, Sirt1/3, NAD<sup>+</sup> pool), upregulate reactive oxygen species (ROS) and autophagy-related genes, which may contribute to the enhanced EV biogenesis (de Almeida Fuzeta et al., 2020; Jeske et al., 2023). It was also observed that some therapeutically relevant protein and microRNA cargo were promoted in the EVs produced in the VWBRs (Jeske et al., 2023). Our previous studies also have isolated and characterized hPSC-derived EVs, including undifferentiated hPSCs, forebrain organoids, cerebellar organoids, choroid plexus organoids and retinal organoids, mostly in static culture (Arthur et al., 2023; Hua et al., 2022; Liu et al., 2022; Marzano et al., 2019, 2021; Muok et al., 2023). Given the potential needs for animal and clinical studies, the biomanufacturing of hPSC-EVs in a scalable bioreactor such as VWBRs has become important.

In this study, the EV secretion by undifferentiated hiPSCs expanded as 3-D aggregates and on Synthemax II microcarriers coated with Matrigel in VWBRs were investigated. The hypothesis of this study is that different 3-D architecture (aggregates vs. microcarrier-based) of hiPSCs in VWBRs modulate EV biogenesis and cargo profiles, possibly due to different cellular metabolic status under dynamic microenvironment. Two different EV collection media, mTeSR and home-brew medium (HBM), were also compared. Although hiPSC expansion as 3-D aggregates and on microcarriers in VWBRs have both been shown previously (Borys et al., 2021; Rodrigues et al., 2018), the focus of this study is the investigation of hiPSC-EV production, biogenesis ability and EV cargo profiles (determined by proteomics and microRNA-sequencing) in these two different 3-D culture systems. The correlations among EV secretion, EV protein cargo, EV microRNA cargo, metabolite analysis, cellular metabolic status, transcriptome signatures as well as microRNA profiles of the parent cells (e.g. based on multi-omics analysis) were also analysed. For functional analysis, microglia cells were treated with VWBR-generated hiPSC-EVs, and then stimulated proliferation and M2 polarization were examined. This study demonstrates a bioreactor platform and detailed cargo profiles for biomanufacturing of hiPSC-EVs towards pre-clinical studies such as anti-senescence treatment for blood–brain barrier in ischaemic stroke and other neurological disorders.

## 2 | MATERIALS AND METHODS

### 2.1 | hiPSC 2-D planar cultures

hiPSCs (TC-1133) were thawed from a vial of the Matched Research Grade hiPSC Working Cell Bank generated under current good manufacturing practices (cGMP) from Lonza (Walkersville, MD, USA) (Baghbaderani et al., 2015). hiPSCs were re-programmed from human CD34+ umbilical cord blood cells using a non-integrating episomal vector reprogramming method (Certificate of Analysis and Lutheran Hospital Institutional Review Board Approval are available upon request). The hiPSCs cryopreserved in CryoStor CS10 solution (StemCell Technologies Inc., Vancouver, Canada) were thawed and plated into growth factor-reduced Matrigel (BD Biosciences)-coated (1:30) Corning CellBIND T-25 and T-75 flasks (Corning, Corning, NY, USA). Cells were seeded at a density of 5000 cells/cm<sup>2</sup> in mTeSR serum-free media (StemCell Technologies Inc.) and cultured under standard condition (5% CO<sub>2</sub>, 37°C). Media were exchanged daily and cells were harvested on day 3 after incubation for 5 min with 0.05% Trypsin-EDTA (Thermo Fisher Scientific Inc., Waltham, MA, USA). Cells were cultured through two passages and then harvested for inoculation of the VWBRs and 2D control.

### 2.2 | Microcarrier and aggregate-based hiPSC expansion in Vertical-Wheel bioreactors

#### 2.2.1 | Aggregate-based expansion

For expansion of hiPSCs as multi-cellular aggregates, the vessels were filled to the seeding volume with mTeSR media (60 mL for the 0.1L vessels), inoculated at cell densities equivalent to microcarrier-based bioreactors (5000 cells/cm<sup>2</sup>) at  $2.8\text{--}3.3 \times 10^4$  cells/mL, then maintained at the lowest possible agitation (22 rpm) for 24 h to promote cell aggregation. On day 1, vessels were brought up to the working volume of 100 mL and the agitation was adjusted to the experimental value (60 rpm). Half media was exchanged daily in each bioreactor. HBM was formulated with a modification of B8 medium and its composition with eight essential components was reported previously (Dang et al., 2021). The formulation of mTeSR medium was also reported previously (Ludwig et al., 2006). Both media were serum-free and contained little EVs (*i.e.* EV-depleted). To compare between different media formulations for EV collection, complete media change was performed at day 5 with HBM (C1-1) or mTeSR (C1-2) (Figure 1a). The spent media were collected at day 8 for EV isolation.

#### 2.2.2 | Microcarrier-based expansion

Corning® Low Concentration Synthemax® II microcarriers (surface area 360 cm<sup>2</sup>/g, Corning Incorporated) were added to the VWBRs (PBS Biotech Inc., Camarillo, CA, USA) (Yuan et al., 2022) at a concentration of 20 g/L, coated with growth factor-reduced Matrigel (1:30). For 100 mL of working volume, 2 g microcarriers were used, and the total surface area was 720 cm<sup>2</sup>. The bioreactor was inoculated with  $4\text{--}5 \times 10^3$  cells/cm<sup>2</sup> in 100 mL, and the seeding density was  $2.8\text{--}3.4 \times 10^4$  cells/mL. The vessels were filled up to the seeding volume with mTeSR media (60 mL for the 0.1-L vessels). Vessels were maintained at the lowest possible agitation (22 rpm) to suspend the microcarriers for 24 h to promote cell attachment. On day 1, vessels were brought up to the full working volume (100 mL for the 0.1L vessels) and the agitation was adjusted to the experimental value (60 rpm) (Jeske et al., 2023). Half media was exchanged daily in each bioreactor. On day 5, complete media were changed with HBM (C2-1) or maintained with mTeSR (C2-2) for EV collection at day 8 (Figure 1a). Three independent bioreactor runs were performed for both aggregate and microcarrier cultures.

### 2.3 | Aggregate size distribution analysis

Following formation of the aggregates or cell-microcarrier clusters, images were taken daily using a Nikon Eclipse Ti-U inverted microscope and attached DS-Qi1 monochrome digital camera. Images were analysed to calculate the diameters of aggregates or cell-microcarrier clusters. Specifically, the captured images were converted to binary images using ImageJ software (<http://rsb.info.nih.gov/ij>) and analysed with the 'particle analysis tool'. Through particle analysis in ImageJ software, the Feret's diameter of each aggregate in the images can be calculated, which provided the average size of the aggregates or cell-microcarrier clusters ( $n = 5\text{--}10$ ).

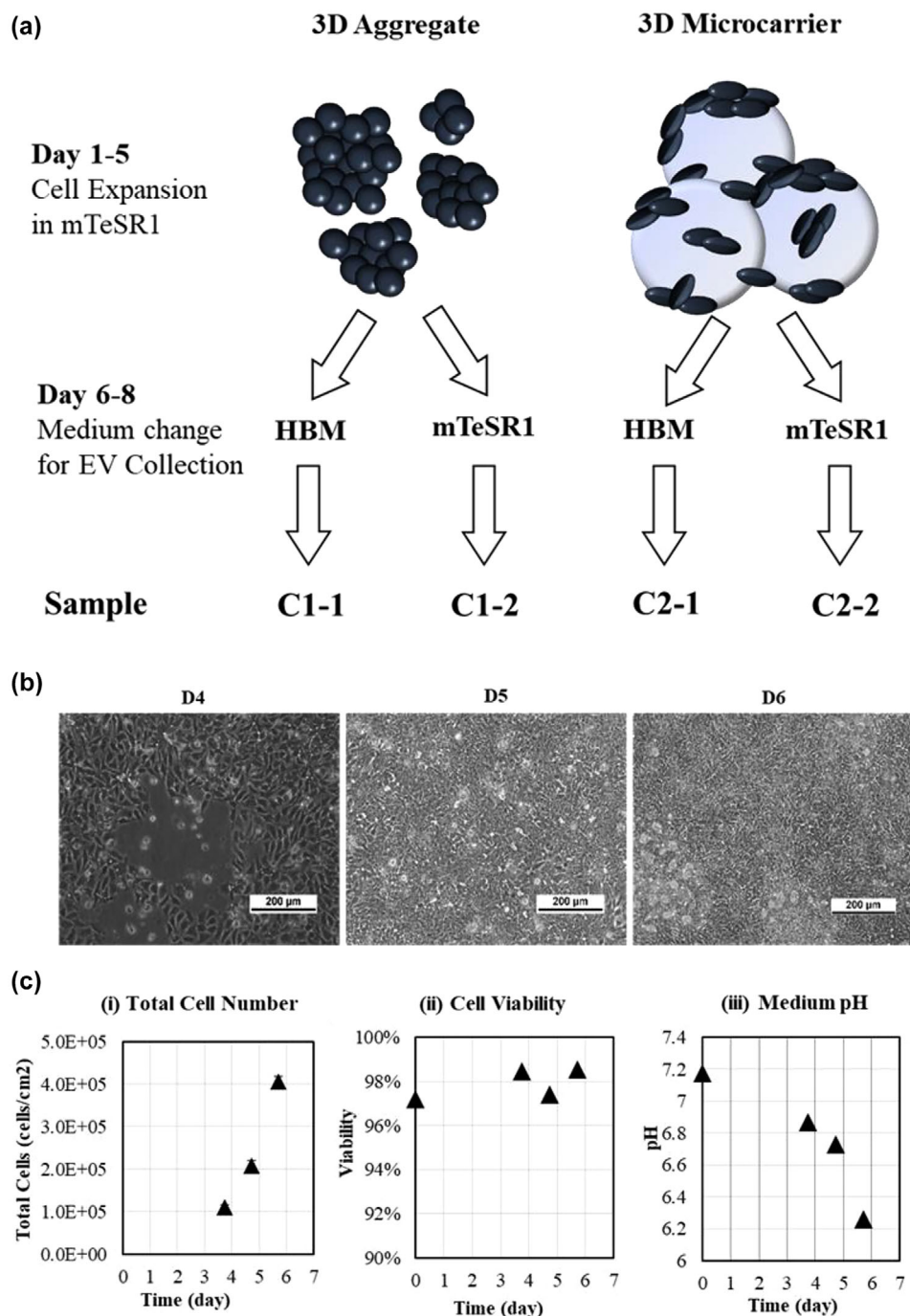


**FIGURE 1** Schematic illustration of 3-D expansion of hiPSCs in Vertical-Wheel bioreactors. (a) Set up of different culture conditions; (b) growth morphology of 2D cultured hiPSCs; (c) culture kinetics of the parent 2D culture of hiPSCs to seed the 3-D cultures. (i) cell number; (ii) viability; (iii) pH values.

## 2.4 | Cell number and metabolite measurements during bioreactor culture

For each bioreactor, samples were taken daily during day 3–8. Three millilitres of cell-containing media samples were removed for microscopic observation, cell counts and metabolite analysis. For cell counts, the cells were spun at 500 g for 5 min. The supernatant was removed and frozen for metabolite analysis. The spent media were analysed with a BioProfile Flex2 (Nova Biomedical, Waltham, MA, USA) analyser for metabolite concentration. The cells were re-suspended in 1 mL (aggregate culture) or 2 mL (microcarrier culture) of Accutase (ThermoFisher), and incubated for approximately 7–10 (microcarriers) and 25 min (aggregates) for cell dissociation. Every 5 min, the tubes containing cell microcarriers were gently swirled to encourage detachment. Following incubation, 1 mL of mTeSR medium was added to the aggregate sample to stop the reaction. For the microcarrier



conditions, samples were strained with a 70- $\mu\text{m}$  pluriStrainer (pluriSelect, El Cajon, CA, USA) to remove microcarriers. The harvested cells were re-suspended in 2 mL of medium and lysed for 30 min with an equal volume of Reagent A100 (ChemoMetec, Bohemia, NY, USA). After lysis, nuclei were stabilized with an equal volume of Reagent B (ChemoMetec, Bohemia, NY, USA). The solution was well mixed and loaded into a Vial-Cassette (ChemoMetec) which was subsequently loaded into a NucleoCounter<sup>®</sup> NC-200 (ChemoMetec) that determined cell concentration. For 2D controls, hiPSCs were washed three times with Dulbecco's phosphate-buffered saline (D-PBS) (Corning Cellgro, Corning, NY, USA) and incubated with Accutase for 5 min at 37°C. The harvested cells were loaded into a Vial-Cassette for counting.

## 2.5 | Cell harvest and EV media collection

At day 8, cell microcarriers or the aggregates were allowed to settle for 10 min without agitation. Conditioned media were then collected and stored at  $-80^{\circ}\text{C}$  for EV isolation. Bioreactors were filled to 50% working volume with D-PBS and agitated at 25 rpm for 90 s. Cell-adhered microcarriers were allowed to settle for 10 min and supernatants were removed. After washing three times, 50% of the D-PBS was removed and replaced with an equal volume of Accutase and incubated at 37°C for 25 min. An equal volume of media was added to quench Accutase and the microcarriers were allowed to settle. Supernatants containing cells were then collected and an additional rinse of D-PBS (25% of working volume) was added to vessels agitated at 25 rpm for 90 s. Microcarriers were allowed to settle and supernatants were pooled together for centrifugation. For aggregate culture, the cells were incubated with Accutase at 37°C for 7–10 min. The cells were suspended in FreSR-S cryopreservation medium (StemCell Technologies Inc.) and then stored at  $-80^{\circ}\text{C}$  for further analysis.

## 2.6 | EV isolation by ExtraPEG-based ultracentrifugation

To isolate the hiPSC EVs, the differential ultracentrifugation method was performed as previously described (Jeske et al., 2023; Marzano et al., 2019; Rider et al., 2016). Briefly, the conditioned media were centrifuged at 500  $g$  for 5 min at 4°C. The supernatants were collected and centrifuged again at 2000  $g$  for 10 min. The collected supernatants were then centrifuged at 10,000  $g$  for 30 min. After the final centrifugation, supernatants were collected and mixed with polyethylene glycol (PEG) solution (16% wt/vol in 1 M NaCl) at a 1:1 volume and incubated at 4°C overnight. The mixed solutions were centrifuged at 3000  $g$  for 1 h. The crude EV pellets were re-suspended in EV-free PBS and then ultra-centrifuged at 100,000  $g$  for 70 min. Purified EV pellets were re-suspended in 100- $\mu\text{L}$  PBS and stored at 4°C or  $-80^{\circ}\text{C}$  for future analysis.

## 2.7 | Nanoparticle tracking analysis (NTA)

NTA was performed on the isolated EV samples in triplicate to determine size distribution and particle concentration, using a Nanosight LM10-HS instrument (Malvern Instruments, Malvern, UK) configured with a blue (488 nm) laser and sCMOS camera (Rider et al., 2016). The EV samples were diluted to 1–2- $\mu\text{g}$  protein per mL in PBS. For each replicate, three videos of 60 s were acquired with camera shutter speed fixed at 30.00 ms. To ensure accurate and consistent detection of small particles, the camera level was set to 13, and the detection threshold was maintained at 5. The laser chamber was cleaned thoroughly with particle-free water between each sample reading. The collected videos were analysed using NTA3.0 software to obtain the mode and mean size distribution, as well as the concentration of particles per millilitre of solution. Compared to the mean size, the mode size is usually a more accurate representation because the vesicle aggregates may affect the value of mean size.

## 2.8 | Transmission electron microscopy (TEM)

TEM was performed to confirm the morphology of EVs according to Lasser et al. (2012) and as shown in our previous publication (Marzano et al., 2019). Briefly, EV isolates were re-suspended in 50–100  $\mu\text{L}$  of sterile filtered PBS. For each sample preparation, intact EVs (5  $\mu\text{L}$ ) were dropped onto Parafilm. A carbon-coated 400 Hex Mesh Copper grid (Electron Microscopy Sciences, EMS) was positioned using forceps with coating side down on top of each drop for 1 h. Grids were washed with sterile filtered PBS three times and then the EV samples were fixed for 10 min in 2% paraformaldehyde (PFA) (EM Grade). After washing, the grids were transferred on top of a 20- $\mu\text{L}$  drop of 2.5% glutaraldehyde (EM Grade) and incubated for 10 min. Grid samples were stained for 10 min with 2% uranyl acetate (EMS grade). Then the samples were embedded for 10 min with 0.13% methyl cellulose and 0.4% uranyl acetate. The coated side of the grids was left to dry before imaging on the Hitachi HT7800 electron microscope (Lasser et al., 2012) at Florida State University.

## 2.9 | Western blotting for EV markers

EV and cell samples were lysed in radio-immunoprecipitation assay (RIPA) buffer (150-mM sodium chloride, 1.0% Triton X-100, 0.5% sodium deoxycholate, 0.1% sodium dodecyl sulphate, 50-mM Tris, pH8 and 1X Thermo Scientific™ Halt™ Protease Inhibitor Cocktail) (Thermo Fisher Scientific Inc., Waltham, MA, USA). Samples were incubated for 20 min on ice, and spun down at 14,000 rpm for 20 min. The cleared supernatants were collected and a Bradford assay was carried out to determine protein concentration. Protein lysate concentration was normalized, and denatured at 100°C in 2 × Laemmli Sample buffer for 5 min. About 3–10 µg of proteins were loaded into each well. Proteins were separated by 12% Bis-Tris-SDS gels and transferred onto a nitrocellulose membrane (Bio-Rad, Hercules, CA, USA). For the detection of non-phosphorylated proteins, the membranes were blocked for 1 h in 1% w/v non-fat dry milk in Tris-buffered saline (10-mM Tris-HCl, pH 7.5 and 150-mM NaCl) with 0.1% Tween 20 (v/v) (TBST). Membranes were incubated overnight in the presence of the primary antibodies (Table S1) diluted in blocking buffer at 4°C. Afterwards, the membranes were washed four times with TBST and then incubated with a horseradish peroxidase (HRP)-conjugated secondary antibody at 1:5000 for 1 h. The blots were washed and imaged on the Biorad ChemiDoc Imaging System.

## 2.10 | Reverse transcription and quantitative polymerase chain reaction (RT-qPCR)

Total RNA was isolated from different cell samples (hiPSCs or BV2) using the RNeasy Mini Kit (Qiagen, Valencia, CA) according to the manufacturer's protocol. The isolated RNA samples were further treated with DNA-Free RNA Kit (Zymo, Irvine, CA, USA) to remove genomic DNA contamination (Song et al., 2016). Reverse transcription was carried out according to the manufacturer's instructions using 2 µg of total mRNA, anchored oligo-dT primers (Operon, Huntsville, AL) and Superscript III (Invitrogen, Carlsbad, CA, USA). The software Oligo Explorer 1.2 (Genelink, Hawthorne, NY, USA) was used to design the real-time PCR primers specific for target genes (Table S2). For normalization of expression levels,  $\beta$ -actin was used as an endogenous control. Using SYBR Green PCR Master Mix (Applied Biosystems, Foster City, CA, USA), real-time PCR reactions were performed on an ABI7500 instrument (Applied Biosystems). The amplification reactions were performed as follows: 2 min at 50°C, 10 min at 95°C, and 40 cycles of 95°C for 15 s and 55°C for 30 s and 68°C for 30 s following with a melt curve analysis. The Ct values of the target genes were firstly normalized to the Ct values of the endogenous control  $\beta$ -actin. The corrected Ct values were then compared for the bioreactor conditions to the 2D control, or between the compared samples. Fold changes in gene expression were calculated using the comparative Ct method to obtain the relative expression levels.

## 2.11 | Proteomics analysis of hiPSC-EV protein cargo

The hiPSC EVs (from the C1-2, C2-1 and C2-2 groups) were isolated using the ExtraPEG method described above and then extracted for proteins, together with the parent cells. Based on the protein quantification result, up to 40-µg proteins were isolated on S-trap micro column (Protifi, K02-micro). The isolated proteins (triplicate for each group) were alkylated and digested on a column based on manufacturer's instructions. All the eluted peptides were fractionated by Pierce high pH reverse phase peptide fractionation kit (Thermo, 84868) into five fractions for each sample. Then all the samples (three replicates) were vacuumed dried and submitted to FSU Translational Science Laboratory for Liquid Chromatography Tandem Mass Spectrometry (LC-MS/MS). The samples were analysed on the Thermo Q Exactive HF as previously described (Hurwitz & Meckes, 2017; Hurwitz et al., 2018). Briefly, resulting raw files were searched with Proteome Discoverer 2.4 using SequestHT, Mascot and Amanda as search engines. Scaffold (version 5.0) was used to validate the protein and peptide identity. Peptide identity was accepted if Scaffold Local false discovery rate (FDR) algorithm demonstrated a probability greater than 99.0%. Likewise, protein identity was accepted if the probability level was greater than 99.0% and contained a minimum of two recognized peptides. Gene Ontology (GO) annotation was carried out by g:Profiler.

## 2.12 | Transcriptome analysis for bioreactor-expanded hiPSC by RNA-sequencing (RNA-seq)

Total RNA from bioreactor-expanded hiPSC samples were isolated by Trizol reagent (ThermoFisher; 15596018) and incubated with DNase I to remove trace genomic DNA contamination before quantified by nanodrop. Then, mRNA-seq library was prepared by combination of NEBNext Ultra RNA Library Prep Kit (NEB, E7530) and NEBNext Poly(A) mRNA Magnetic Isolation Module (NEB, E7490). The constructed libraries were run on a Bioanalyzer with HS DNA chip (Agilent; 5067–4626) for quality control and finally quantified by KAPA library quantification kit (KAPA; KR0405). Then the libraries were pooled at equal molar

amounts and submitted to the Florida State University College of Medicine Translational laboratory for sequencing on illumina NovaSeq 6000 system.

### 2.13 | Small RNA profiling analysis of hiPSC-EVs by RNA-seq

EV-associated miRs were isolated and sequenced using the protocol below. Each sample was analysed in triplicate. EV samples were treated with RNase (ThermoFisher; AM2294) at a final concentration of 50 ng/mL, at room temperature for 30 mins. RNase inhibitor (NEB; M0314) and PCR grade water were added to EV samples to make a total volume of 200  $\mu$ L. miRs were isolated by adding 600  $\mu$ L Trizol LS (ThermoFisher; 10296010) according to the manufacturer's instruction. To increase the yield of small RNAs, three volumes of 100% ethanol and linear acrylamide (VWR; 97063–560) were used instead of isopropyl alcohol and incubation time was also increased to overnight at  $-20^{\circ}$ C. The isolated RNAs were quantified by Qubit microRNA assay kit (ThermoFisher; Q32880). Small RNA libraries were generated with NEBNext Multiplex Small RNA Library Prep Set for Illumina (NEB; E7300). To increase yield and prevent primer/adaptor dimer, 3' SR primer was diluted to 1:5 and increase ligation time to overnight at  $16^{\circ}$ C. Similar to mRNA-seq library preparation, HS DNA chip and KAPA library quantification kit were used before submitting to sequencing by illumina NovaSeq 6000 in Florida State University College of Medicine Translational lab.

### 2.14 | RNA-seq data analysis

Raw data for miR-seq were submitted to the OASIS online miR analysis tool to identify small RNAs on Human reference genome hg38. Differentially expressed miRs were analysed by both OASIS and miRNet using default settings. RNA-seq data were analysed by ExpressAnalyst (Liu, 2023). Genes with counts less than 10, variance less than 10% and unannotated were filtered and normalized by Log<sub>2</sub>-counts per million. Differentially expressed genes (DEGs) were identified by DEseq2. Heatmap of globe differential expressed genes and gene-enriched pathways were also visualized by the same online tool.

### 2.15 | BV2 microglia proliferation and function assays

Mouse microglia cell line BV2 from American Type Culture Collection (ATCC) was used in our study to investigate the function of hiPSC-EVs. BV2 cells were maintained at  $37^{\circ}$ C and 5% CO<sub>2</sub>. The Dulbecco's modified Eagle's medium (DMEM) was supplemented with a 10% heat-inactivated foetal bovine serum (FBS; Seradigm; 1400–500) and 100 IU penicillin-streptomycin (Corning; 30-002-CI). BV2 cells were seeded in 96-well plate and treated with equal amounts ( $1 \times 10^8$ ) of hiPSC-EVs at the same time. After 3–4 days, cell mass was quantified by the standard Sulforhodamine B (SRB) assay (Vichai & Kirtikara, 2006). Before re-dissolving the dye into Tris-buffer, bright field microscopy images were captured to clearly view cell morphology and density. For the function assay, BV2 cells were seeded at  $3 \times 10^5$  cells/well in 24-well plate with hiPSC-EVs. After 24 and 72 h, cells were harvested with Trizol reagent for total RNA isolation and RT-qPCR analysis.

### 2.16 | Statistical analysis

Three independent bioreactor runs were performed. Experimental results were expressed as means  $\pm$  standard deviation (SD). Statistical comparisons were performed by one-way ANOVA and Tukey's post hoc test for multiple comparisons, and significance was accepted at  $p < 0.05$ . For comparisons of two conditions, student's *t*-test was performed for the statistical analysis.

## 3 | RESULTS

### 3.1 | hiPSC expansion in Vertical-Wheel bioreactors

Three independent bioreactor runs were performed and the Run 2 data are shown as the representative results. The 2D hiPSCs were seeded directly in suspension to form aggregates (C1-1 in HBM, C1-2 in mTeSR) or onto microcarriers (C2-1 in HBM, C2-2 in mTeSR) in VWBRs (Figure 1a). These four condition codes were used for blind test purpose. The cultures were expanded in mTeSR during day 1–5. On day 5, the HBM or mTeSR was used until day 8 for EV collection. The 2D parent cells showed normal colony morphology, and the colony size increased over the culture period (Figure 1b). Additionally, cell count, viability and pH were measured (Figure 1c). On day 3, the cell number was approximately  $1.1 \times 10^5$  cells/cm<sup>2</sup> and increased to  $4.1 \times 10^5$  on day 5

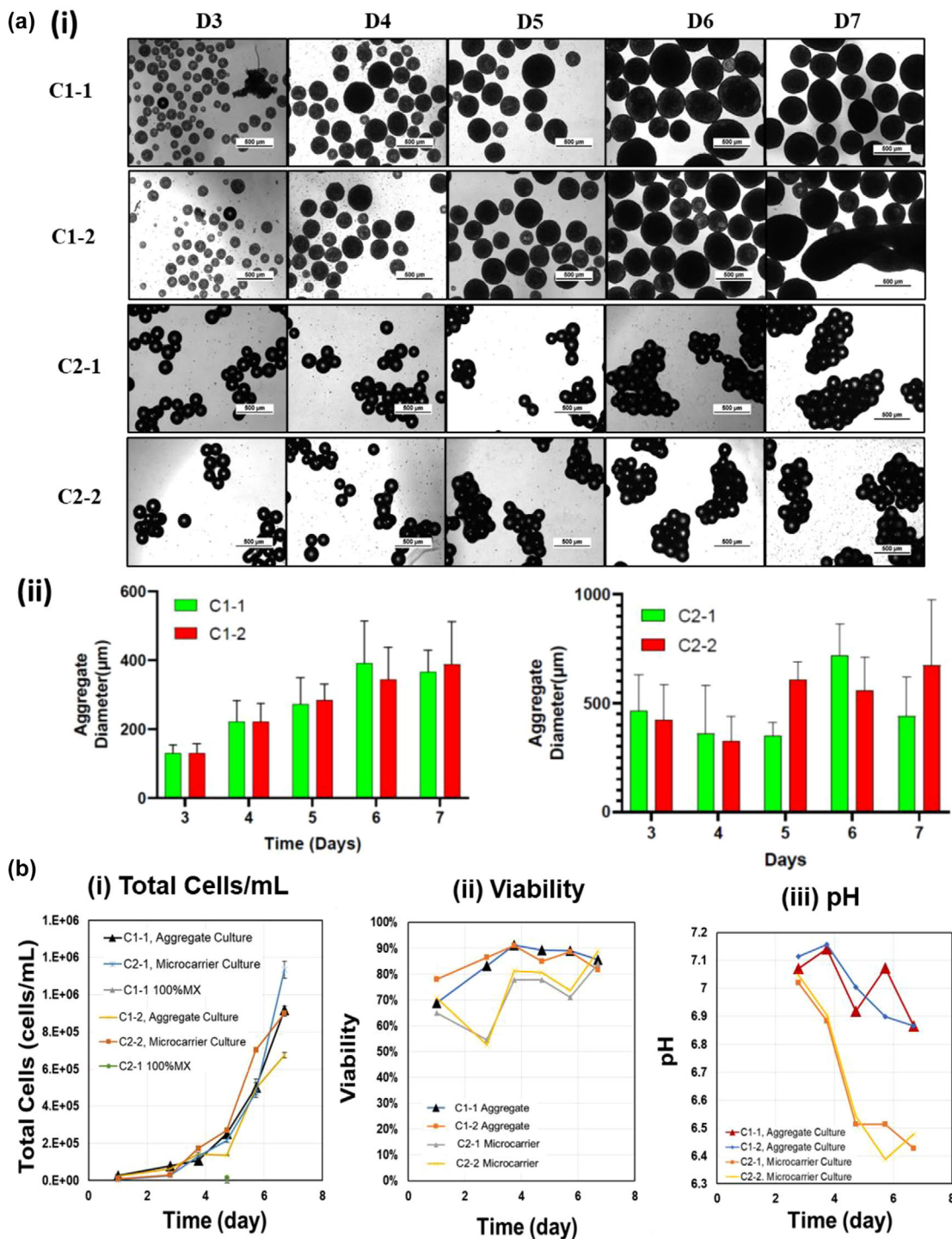


**FIGURE 2** Culture morphology and expansion kinetics of 3-D expansion of hiPSCs in Vertical-Wheel bioreactors. (a) (i) hiPSC aggregates and on microcarriers morphology over the culture time; (ii) kinetics of average aggregate size analysed by image analysis; (b) growth kinetics for 3-D expansion of hiPSCs (Run 2 data). (i) Cell number; C1-1 and C2-1 media were counted as negative controls. (ii) Viability; (iii) pH values.

(a 27-fold expansion compared to seeding density). The viability remained high (97%–99%) during the culture. The pH showed a drop from 7.18 on day 0 to 6.26 on day 5.

The four bioreactor conditions were sampled daily during day 3–7 for cell morphology, cell number, viability and pH. From the images, the aggregate size increased over the time ( $\sim 150 \mu\text{m}$  at day 3 to  $\sim 400 \mu\text{m}$  at day 7) (Figures 2a and S1). For the microcarrier conditions, several microcarriers with cells formed clusters, which also increased with culture time ( $\sim 400 \mu\text{m}$  at day 3 to  $\sim 1 \text{ mm}$  at day 7). There were no significant differences in aggregate or cluster diameter for the two media conditions. For



the growth kinetics, all four conditions showed similar trends and significant growth during day 1–7 (Figure 2b). On day 7, C1-1 had a cell density of  $0.92 \times 10^6$  cells/mL (33-fold expansion), and C1-2 with  $0.67 \times 10^6$  cells/mL (29-fold expansion). C2-1 had a cell density of  $1.1 \times 10^6$  cells/mL (29-fold expansion) and C2-2 with  $0.9 \times 10^6$  cells/mL (30-fold expansion). Overall, the expansion did not seem to depend on microcarrier or aggregate cultures. During day 3–6, the aggregate conditions had high viability of 69%–91% compared to the microcarrier conditions of 53%–81%. On day 7, the viability was similar for all four conditions (82%–89%). The low cell viability in some groups may be due to the harsh cell dissociation process prior to the cell counting, which may be dependent on individual sample preparation. The pH values displayed a drop from 7.0–7.1 to 6.4–6.8. The pH values for the aggregate samples (6.87–7.16) were higher than the microcarrier samples (6.39–7.05). Overall, aggregate cultures increased in size over time while microcarrier cultures showed relatively constant clumping of carriers and a large drop in pH over time.

Metabolite analysis of bioreactor cultures was performed (Figure 3). For glucose metabolism (Figure 3a), the glucose concentration decreased much more for microcarrier cultures (from 12 to ~4 mM) compared to aggregate cultures (from 12 to 8–10 mM). Correspondingly, lactate production was much higher for microcarrier cultures (~18–22 mM) compared to aggregate cultures (~10 mM). The lactate to glucose (mol/mol) ratio was calculated and the aggregate cultures had a lower value (C1-1:  $1.64 \pm 0.08$  and C1-2:  $1.58 \pm 0.08$ ) than the microcarrier cultures (C2-1:  $1.79 \pm 0.08$  and C2-2:  $1.77 \pm 0.09$ ) ( $p = 0.037, 0.017$  respectively). For glutamine metabolism (Figure 3b), the glutamine concentration showed a large decrease for the HBM cultures (from 2 to 0.5 mM) (C1-1 and C2-1) compared to mTeSR cultures (from 2 to 1.5 mM) (C1-2 and C2-2) during day 5–8. Before day 5, microcarrier cultures metabolized more glutamine and generated more ammonia than the aggregate cultures. The ammonia to glutamine (mol/mol) ratios showed that aggregate groups had higher values (0.89–0.92) than microcarrier groups (0.83–0.87) ( $p < 0.05$ ) before day 5. After day 5, the media effects become significant. Ion concentrations were also measured ( $\text{Na}^+$ ,  $\text{K}^+$  and  $\text{Ca}^{2+}$ ) (Figure 3c), and indicated that differences primarily occurred during day 5–8, where mTeSR medium (C1-2, C2-2) had higher  $\text{Na}^+$  levels, lower  $\text{K}^+$  and  $\text{Ca}^{2+}$  levels compared to HBM medium (C1-1, C2-1), possibly due to different media formulations for EV collection. Overall, microcarrier culture showed increased consumption of metabolites and more active metabolism.

For Run 1 (Figures S2–S4), hiPSC expansion reached a low cell density ( $0.2\text{--}0.4 \times 10^6$  cells/mL, 5–12 fold expansion) probably due to cell aggregation and microcarrier clumping. All conditions showed comparable performance. The cell viability and pH values were at similar values to Run 2. For the metabolite levels, the lactate-to-glucose ratios were in the range of 1.5–2.0, and the ammonia-to-lactate ratios were in the range of 0.7–0.9. For Run 3 (Figure S5–S7), hiPSCs showed good expansion comparable to Run 2 (22–23 fold expansion for aggregate cultures, 30–32 fold for microcarrier cultures). The cell viability and pH values were similar to Run 2 as well. For metabolite analysis, microcarrier culture had more glucose consumption and lactate production than the aggregate cultures. The lactate-to-glucose ratios were in the range of 1.63–1.76 (no significant differences among different conditions due to large variations), and the ammonia-to-lactate ratios were in the range of 0.9–1.0. Similar to Run 2, during day 5–8, mTeSR medium (C1-2, C2-2) had higher  $\text{Na}^+$  levels, lower  $\text{K}^+$  and  $\text{Ca}^{2+}$  levels compared to HBM medium (C1-1, C2-1). The expansion performance of the three runs was summarized in Table S3.

### 3.2 | Transcriptome analysis of EV biogenesis and metabolism in bioreactor-hiPSCs

Transcriptome analysis was performed based on next-generation sequencing (NGS) data, that is, mRNA-seq, for the hiPSCs expanded in VWBRs (Figure 4 and Excel Data file S1 and S2). Principal component analysis (PCA) showed distinct clusters of C1-1, C1-2, C2-1 and C2-2 cells based on 14,368 identified genes (Figure 4a). DEGs were identified (number of 5123) based on comparisons of C2-2 versus C1-2 (microcarrier vs. aggregate in mTeSR) and shown in Volcano plot (Figure S8A). GO annotation shows pathway analysis of these DEGs (Figure 4b) and identified the top 20 pathways enriched in C2-2 condition, which includes regulation of cellular metabolic process, canonical glycolysis, nervous system development, Wnt signalling pathway, extracellular matrix (ECM) organization, cell cycle, actin cytoskeleton and microtubule organization, cell migration, cellular biosynthetic process, p53 signalling pathway, pathway in cancer, focal adhesion, assembly of collagen fibrils, non-integrin membrane-ECM interaction and hsa-miR19b-3p. Several DEGs related to glycolysis were upregulated in the C2-2 condition (Table 1), such as *HK2*, *PDK1*, *PKM* and *LDHA*.

Kyoto Encyclopaedia of Genes and Genomes (KEGG) pathway analysis of DEGs for microcarrier versus aggregate cultures in mTeSR (C2-2 vs. C1-2) identified the pathways enriched in the C2-2 condition: Hippo signalling, Wnt signalling pathway, miRNAs in cancer, phosphoinositide-3-kinase (PI3K)-Protein kinase B (PKB or AKT) signalling pathway, ECM-receptor interactions, glycolysis and gluconeogenesis, Hypoxia-Inducible Factor (HIF)-1 signalling pathway, Rap1 signalling pathway, insulin section, fructose and mannose metabolism (Figure S8B). These pathway-related DEGs were highly expressed in C2-2 cells, as shown in the Ridgeline diagram of enriched genes (Figure 4c). As an example, heatmap analysis of mammalian target of rapamycin (mTOR) pathway-related DEGs displays the primary differences among the four conditions and indicates that culture type had a much larger influence than media condition (Figure 4d). mTOR and mitogen-activated protein kinase (MAPK)1 were highly expressed in aggregate culture, while Wnt9b and AKT1 were highly expressed in microcarrier cultures. Analysis of EV biogenesis-related genes (*i.e.* *Alix* (*Pdc6ip*),  $-0.14$ ; *TSG101*,  $-0.001$ , *STAM*,  $-0.14$ , *MITF*,  $0.85$ , *SRS* (*SRR*),  $-0.13$ , *SMPD2*,  $-0.43$ , *SMPD3*,  $0.13$ , *Rab27A*,  $-0.15$ , *Rab27B*,  $0.026$ ), indicated relatively small differences and these genes were generally comparable for C2-2 versus

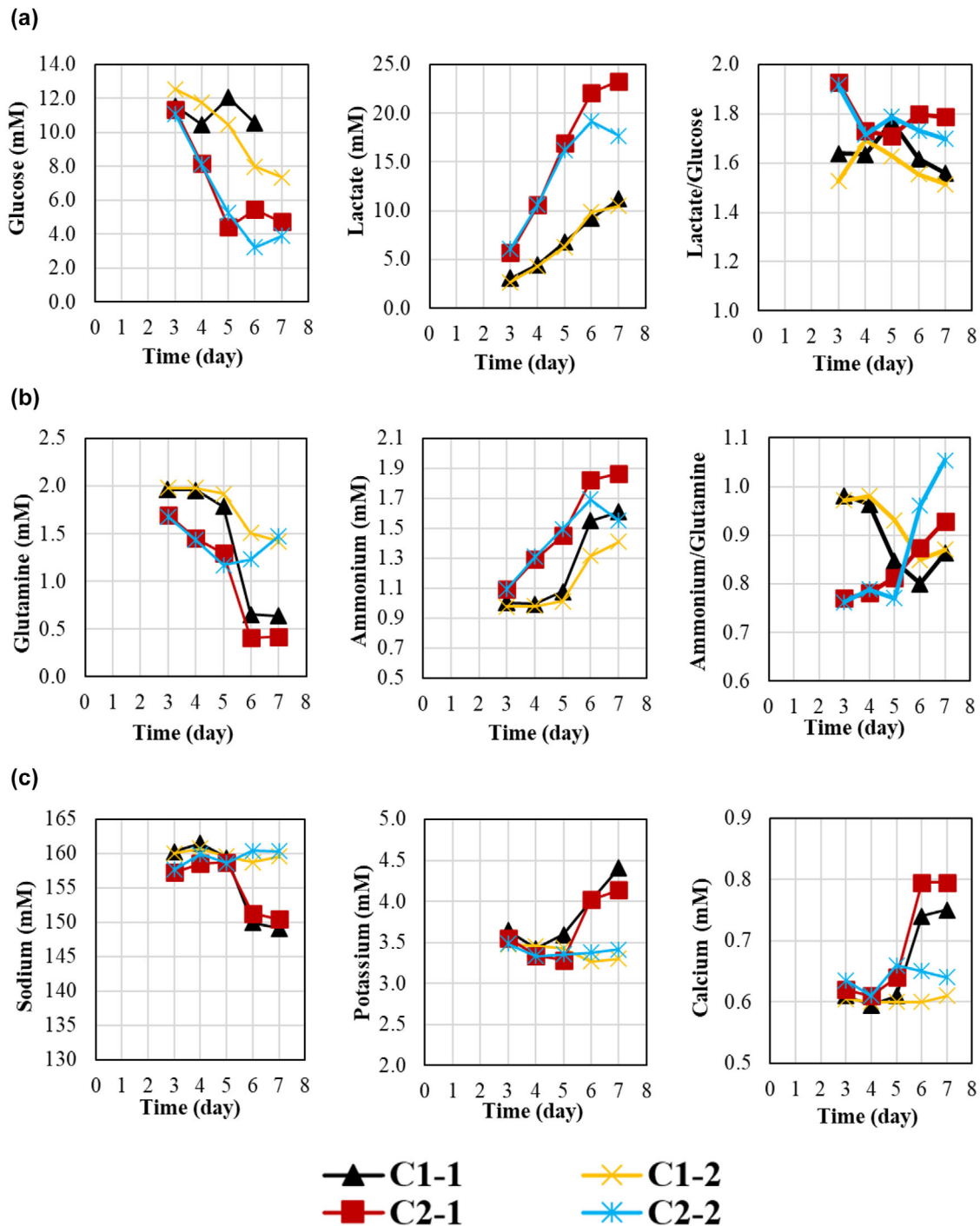


**FIGURE 3** Metabolite analysis of the 3-D expansion of hiPSCs in Vertical-Wheel bioreactors. (a) Glucose metabolism: glucose concentration, lactate concentration; lactate/glucose mol/mol ratio; (b) glutamine metabolism; glutamine concentration, ammonia concentration; ammonia/glutamine mol/mol ratio; (c) ion ( $\text{Na}^+$ ,  $\text{K}^+$ ,  $\text{Ca}^{2+}$ ) concentration: distinct different levels were observed after day 5 for two types of EV collection media. (Run 2 data).

C1-2 (Data S1). *CD9* (0.75), *CD63* (0.22) and *CD81* (0.34) were slightly higher for C2-2 condition. Pluripotency-related genes indicated slightly higher expression for C2-2 compared to C1-2 for *NANOG* (0.78) and *POU class 5 homeobox 1 (OCT4)* (0.12). C2-2 showed significantly higher expression of *VEGFA* (2.45), *Noggin* (2.89), *PDGFB* (4.93), *EGF* (1.13), *IGF2* (1.34) and *TGFBI* (0.50) than C1-2 condition. Overall, these results indicate the upregulation of glycolysis, cell-ECM signalling, growth factor secretion and so forth for microcarrier culture compared to aggregate culture.

For the differences between C2-2 versus C2-1 (mTeSR vs. HBM in microcarrier cultures), the volcano plot showed a total of 253 DEGs (Figure S9). GO annotation shows the pathway analysis of DEGs for C2-2 versus C2-1, which identified the top six

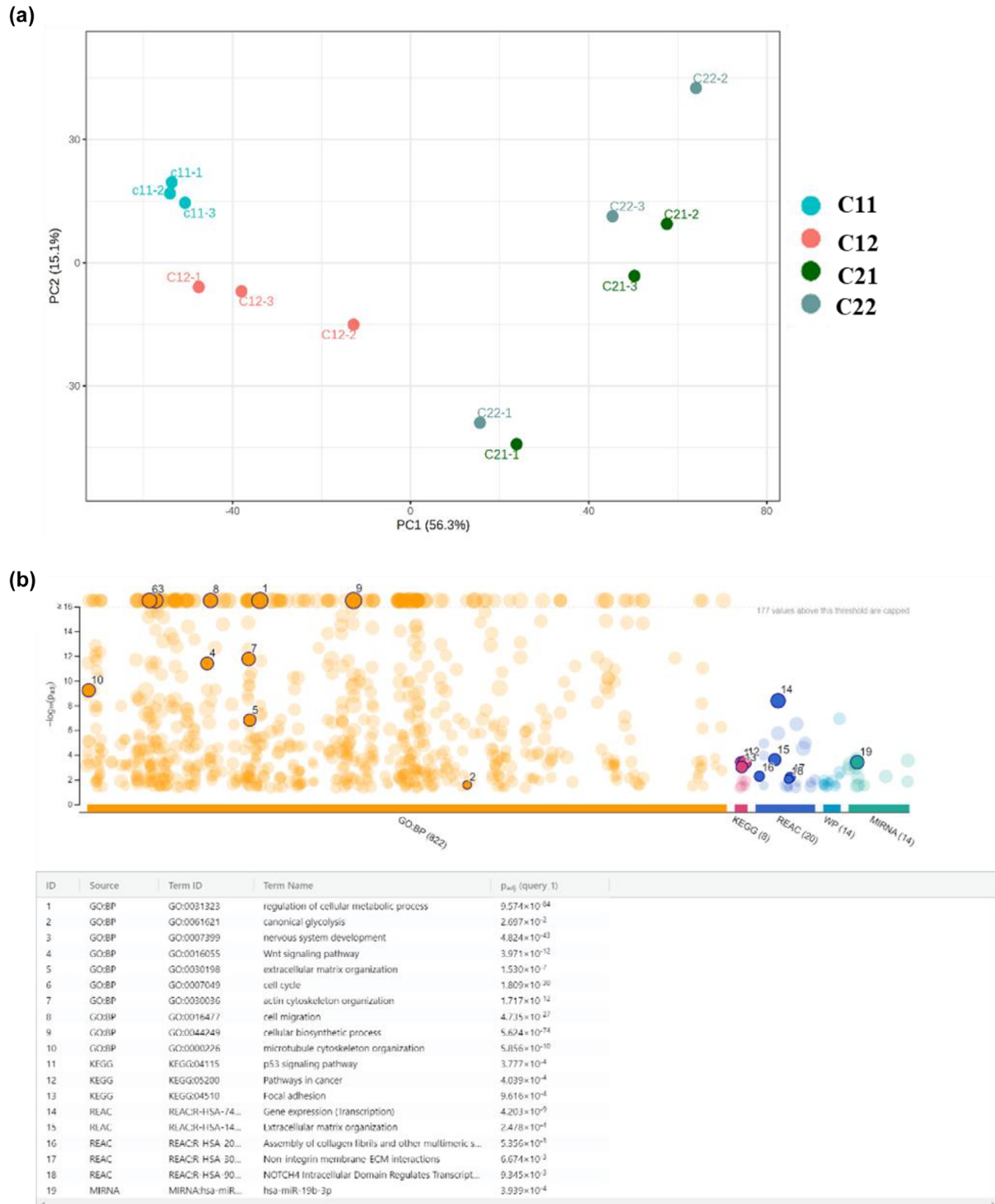


**FIGURE 4** mRNA sequencing of the VWBR-expanded hiPSCs. (a) PCA plots to show the cluster of C1-1, C1-2, C2-1 and C2-2 cells; (b) gene ontology (GO) annotation shows the pathway analysis of DEGs for C2-2 versus C1-2 (microcarriers vs. aggregate cultures) in mTeSR medium; (c) ridgeline diagram of enriched genes for C2-2 versus C1-2. (d) Heatmap illustration of mTOR pathway-related DEGs among the four culture conditions.

pathways including regulation of primary metabolic processes, regulation of cell cycle, Notch pathway and blood vessel development. A Ridgeline diagram of enriched genes shows the enriched pathways in C2-2 versus C2-1, which include microRNAs in cancer, Notch signalling pathway, transforming growth factor (TGF)-beta signalling pathway, HIF-1 signalling pathway, IL-17, p53, MAPK, AMP-activated protein kinase (AMPK), FoxO signalling pathways and so forth.

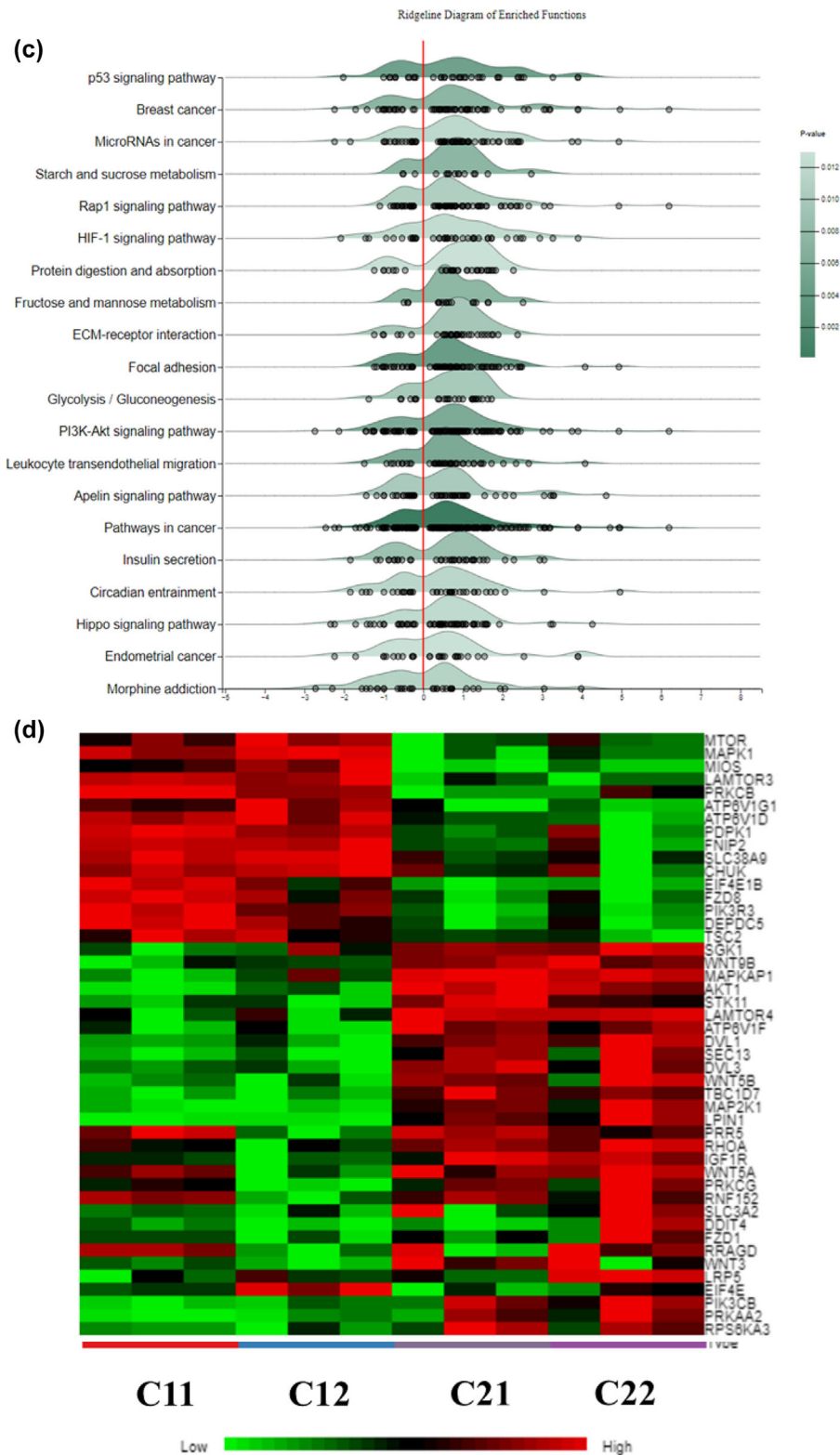
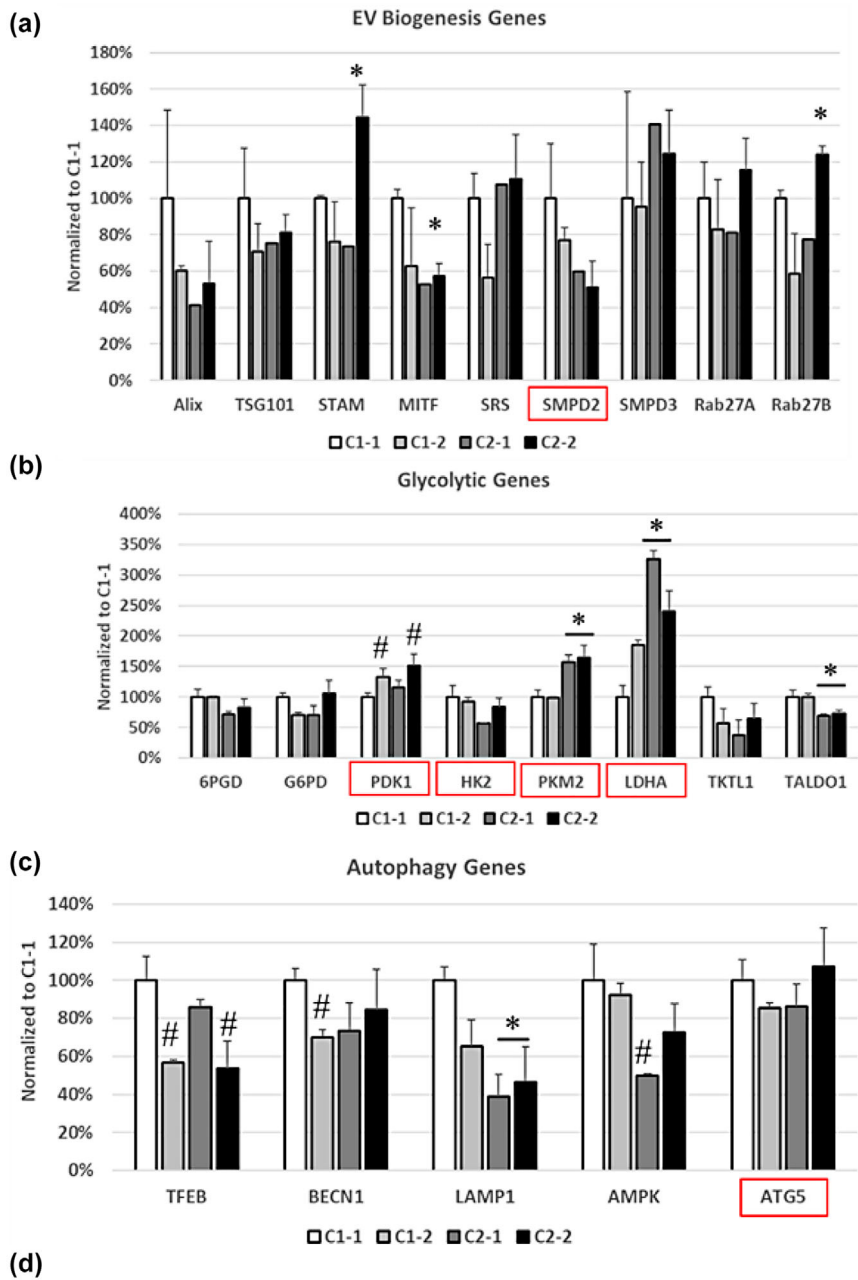


FIGURE 4 Continued

RT-qPCR was performed for EV biogenesis genes (Figure 5a), metabolism genes (Figure 5b) and autophagy genes (Figure 5c). The endosomal sorting complexes required for transport (ESCRT)-dependent exosomal markers include *Alix*, *TSG101* and *SRS*. *SMPD2* and *SMPD3* hydrolyse sphingomyelin that generates EVs in an ESCRT-independent manner. The GTPase *Rab27A* has functions in multivesicular endosomal docking to the plasma membrane. There were no significant differences among the four conditions for *Alix*, *TSG101*, *SRS*, *SMPD2*, *SMPD3* and *Rab27A* (Figure 5a). *Stam* is ESCRT-dependent and shows the upregula-



**FIGURE 5** RT-qPCR analysis of EV biogenesis, metabolism and autophagy gene expression in bioreactor-expanded hiPSCs. (a) EV biogenesis marker expression; \* indicates  $p < 0.05$  compared to other conditions. (b) Metabolic gene expression; \* and # indicate  $p < 0.05$  compared to the C1-1 condition. (c) Autophagy gene expression. (d) Same genes in (a–c, boxed in red) were also found in mRNA-seq results (C2-2 vs. C1-2). \* and # indicate  $p < 0.05$  compared to the C1-1 condition. ( $n = 3$ ).



**TABLE 1** Glycolysis-related genes from mRNA-sequencing GO:BP 0061621 (C2-2 vs. C1-2). The positive values indicate the upregulation in the C2-2 condition, microcarrier in mTeSR compared to aggregates in mTeSR.

Name	Symbols	logFC	Adj.p.val
Pyruvate kinase M1/2	PKM	1.2	4.8E-14
Phosphoglycerate kinase 1	PGK1	1.4	2.4E-09
Phosphofructokinase, platelet	PFKP	0.6	3.2E-07
Hexokinase 1	HK1	1.3	1.1E-06
Hexokinase 2	HK2	1.6	1.9E-05
Forkhead box K1	FOKK1	1.2	1.6E-04
Forkhead box K2	FOKK2	0.2	1.7E-02
Enolase 1	ENO1	0.5	3.2E-04
Enolase 2	ENO2	1.0	8.7E-03
Phosphofructokinase, liver type	PFKL	0.4	5.1E-03
Triosephosphate isomerase 1	TPI1	0.4	8.3E-03
Glucokinase	GCK	0.9	4.1E-02

**TABLE 2** A summary of total numbers and the relative ratios of the isolated hiPSC-EVs from 50 mL spent medium.

Conditions	Run 1	Run 2	Run 3
C1-1	1.28E+08	7.00E+09	1.80E+09
C1-2	2.00E+08	1.90E+10	5.80E+09
C2-1	3.36E+09	1.20E+11	4.00E+11
C2-2	6.24E+09	4.40E+11	5.20E+11
C2-1/C1-1	26.2	17.1	222.2
C2-2/C1-2	31.2	23.2	89.7
C1-2/C1-1	1.6	2.7	3.2
C2-2/C2-1	1.9	3.7	1.3

tion in C2-2 group compared to the other three conditions. *Rab27B* (similar function to *Rab27A*) was also upregulated for the C2-2 group compared to the other three conditions. *MITF* is a driver of melanin synthesis and can activate the transcription of MET, an important receptor tyrosine kinase involved in EV release. C2-2 showed the downregulation compared to the C1-1 condition (confirmed by mRNA-seq). The VWBR-expanded hiPSCs were measured for genes responsible for activating and regulating key steps in glycolysis and pentose phosphate pathway, including *6PGD*, *P6GD*, *PDK1*, *HK2*, *PKM2*, *LDHA*, *TKTL1* and *TALDO1* (Figure 5b). *PKM2* and *LDHA* showed the upregulation for the microcarrier conditions compared to aggregate conditions. *TALDO1* showed slight downregulation. *PDK1* seemed to be affected by the EV collection medium and mTeSR medium conditions showed upregulation. mRNA levels integral to key functions of autophagy were also determined, including *TFEB*, *BECN1*, *LAMP1*, *AMPK* and *ATG5* (Figure 5c). Transcription factor *TFEB* is involved in boosting lysosomal biogenesis. *AMPK* is an upstream initiator shown to induce autophagy activation. *BECN1*, *LAMP1* and *ATG5* are the key in autophagic vesicle formation, lysosomal integrity and membrane trafficking. *TFEB* seemed to be affected by the EV collection medium and mTeSR condition showed the downregulation compared to HBM condition. *LAMP1* showed the upregulation for the microcarrier conditions compared to C1-1 condition. *BECN1* was the lowest for C1-2 condition and *AMPK* was the lowest for the C2-1 condition. The results from mRNA-sequencing (C2-2 vs. C1-2) were consistent with the RT-qPCR results (Figure 5d). Overall, these results indicate that a couple of EV biogenesis genes are influenced by culture condition and that microcarrier culture in mTeSR media likely provides the most stimulation of EV biogenesis.

### 3.3 | EV isolation, characterizations and protein cargo analysis

EVs were isolated from the four conditions and NTA was performed for each run (Figures 6 and S10, and Tables 2, 3, S4 and S5). From 50-mL spent medium, in all three runs, C1-1 generated the least amount of EVs, followed by C1-2, C2-1 and C2-2 generated the most amount of EVs. Microcarrier conditions generated 17–222 fold (for C2-1/C1-1) and 23–90 fold (for C2-2/C1-2) more EVs

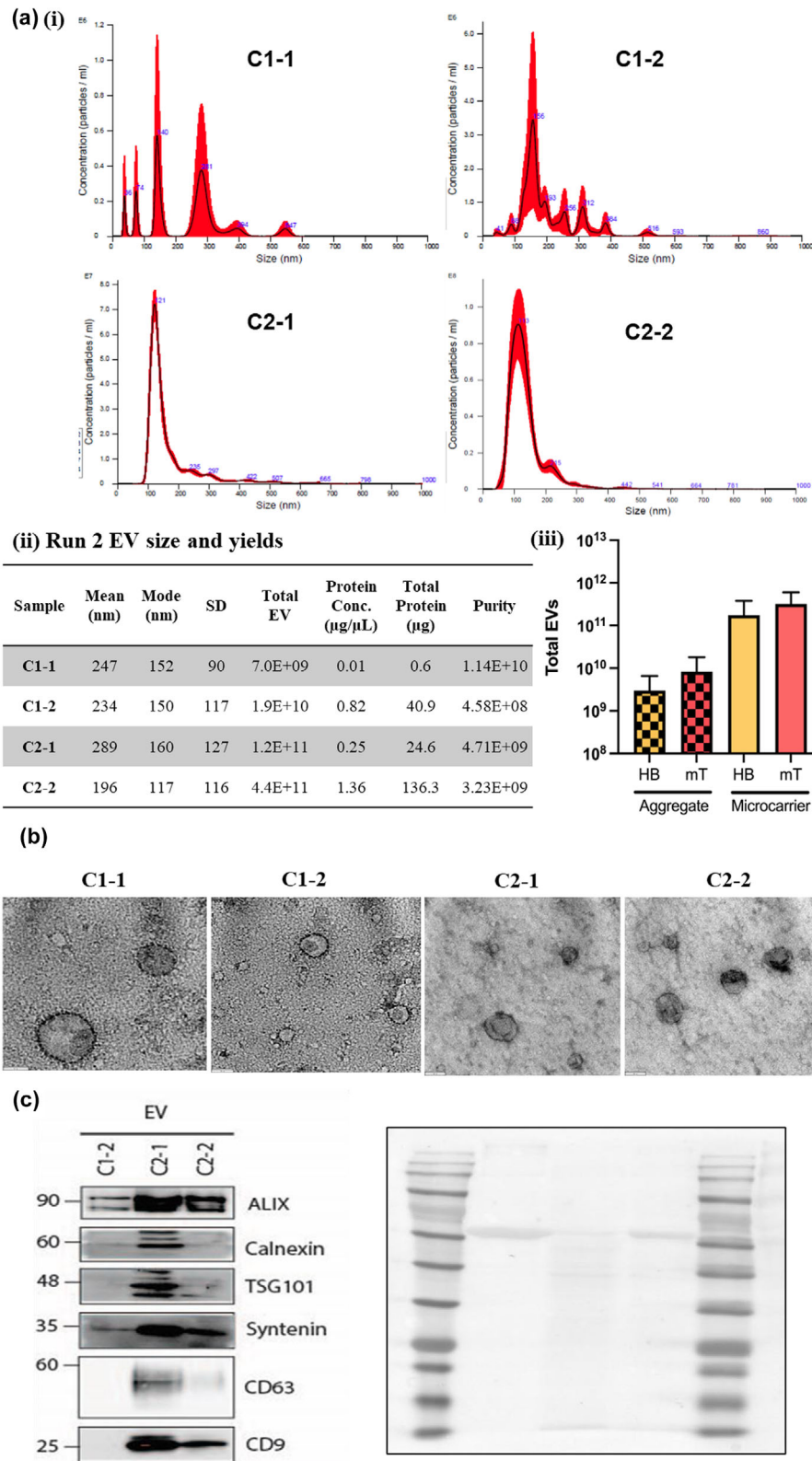


**FIGURE 6** hiPSC-EV characterizations and production yields. (a) Nanoparticle tracking analysis; (i) the representative particle size distribution (Run 2); (ii) EV yield, protein content and purity (Run 2). (iii) The average total EVs produced from the bioreactors ( $n = 3$  independent bioreactor runs). HB: HBM; mT: mTeSR. The plot is on the Log scale and microcarrier versus aggregate samples were statistically significant from each other ( $p < 0.05$ ). (b) Transmission electron microscopy images to show exosome morphology; (c) western blot assay of exosomal markers. Ponceau S staining for total protein is on the right. C1-1 group was not analysed due to the insufficient EV amount.

**TABLE 3** A summary of the mode size of the isolated hiPSC-EVs.

Conditions	Run 1	Run 2	Run 3	Average	SD
C1-1	140	152	122	137.9	15.1
C1-2	163	150	145	152.7	9.4
C2-1	121	160	133	137.8	20.2
C2-2	112	117	118	115.7	3.2

**TABLE 4** Wnt-related pathway for C1-2 and C2-2 comparison (microcarrier vs. aggregate in mTeSR).

Identified proteins	Accession number	T-test (p-value)	Fold change	Quantitative profile
Na(+)/H(+) exchange regulatory cofactor NHE-RF1	O14745	0.017	INF	C1-2 low, C2-2 high
Collagen alpha-1(I) chain	P02452	0.016	INF	C1-2 low, C2-2 high
Tyrosine-protein kinase Yes	P07947	<0.00010	INF	C1-2 low, C2-2 high
Serine/threonine-protein phosphatase 2A 65-kDa regulatory subunit A alpha isoform	P30153	0.00026	15	C1-2 low, C2-2 high
Cell division control protein 42 homolog	P60953	0.0018	INF	C1-2 low, C2-2 high
Transforming protein RhoA	P61586	0.033	4.8	C1-2 low, C2-2 high
Vacuolar protein sorting-associated protein 35	Q96QK1	0.037	INF	C1-2 low, C2-2 high
DNA damage-binding protein 1	Q16531	0.0041	INF	C1-2 low, C2-2 high
Histone deacetylase 2	Q92769	0.00012	INF	C1-2 low, C2-2 high
ATP-dependent RNA helicase DDX3X	O00571	0.019	0.3	C1-2 high, C2-2 low
Apolipoprotein E	P02649	0.00084	0.3	C1-2 high, C2-2 low
Fibroblast growth factor 2	P09038	0.0015	0.2	C1-2 high, C2-2 low

in HBM collection or mTeSR collection, respectively, than the corresponding aggregate conditions (Table 2). For microcarrier conditions, mTeSR collection generated 1.30–3.67 fold (C2-2/C2-1) more EVs than HBM collection. For aggregate conditions, mTeSR collection generated 1.56–3.22 fold (C1-2/C1-1) more EVs than HBM collection. The EV size distribution was shown by NTA (Figure 6a). The mode size (112–163 nm) is usually a more accurate representation of the EV size as vesicle aggregates affect the mean size (196–289 nm). The C2-2 condition had significantly smaller size ( $115.7 \pm 3.2$  nm) than the other three conditions (138–152 nm). The sub-population of small-size EVs (also called as exosomes) has been considered more therapeutically relevant (Deng et al., 2022; Gao et al., 2022; Xia et al., 2020). From TEM images, typical cup-shaped exosomal morphology was observed for each condition (Figure 6b). Positive exosomal markers ALIX, TSG101, CD63, CD9 and Syntenin were highly positive for C2-1 and C2-2 conditions, but weakly expressed for the C1-2 condition (Figure 6c). The C1-1 condition had insufficient yield and was not analysed. For negative exosomal marker Calnexin, C2-2 had little expression but C2-1 had some expression, indicating contamination of cellular materials and/or apoptotic debris. This may also contribute to the higher expression of positive exosomal markers in C2-1 than C2-2 groups, in which transcriptome analysis indicated higher CD9, CD63 and CD81 for C2-2 group. Taken together, C2-2 condition generated high yield and quality of hiPSC-EVs.

The protein cargo of the isolated hiPSC-EVs was analysed by mass spectrometry of total protein content (Figure 7 and Excel Data file S3). C1-1 analysis was not performed due to the insufficient EV yield. The differentially expressed proteins (DEPs) are shown in a Venn Diagram for C1-2 versus C2-2 (effect of microcarrier vs. aggregate cultures in mTeSR media) and C2-1 versus C2-2 (effect of EV collection medium for microcarrier cultures) (Figure 7a). Among 615 DEPs for the C1-2 group, 573 (93.2%) DEPs were overlapped with the C2-1 group (1372 DEPs) and the C2-2 group (1149 DEPs). There were 553 DEPs overlapping between the C2-1 (40.3%) and C2-2 (48.1%) groups. C2-1 group had the most distinct DEPs (223, 16.3%) among the three groups. GO annotation shows the pathway analysis of DEPs for microcarrier versus aggregate (C2-2 vs. C1-2) with total DEPs-502; C2-2 high-452; C1-2 high-50 (Figure 7b). The identified top pathways include ECM-receptor interaction, focal adhesion, tight junction, ECM organization, Wnt5A-associated pathway, beta catenin-independent Wnt pathway, regulation of apoptosis and cell cycle-related G1/S transition pathway. The specific protein cargo related to the Wnt pathways (e.g. collagens, FGF2) is shown in Table 4 and the negative regulation of apoptosis-related proteins is shown in Table 5.

GO annotation also shows the pathway analysis of DEPs for different EV collection medium for microcarrier cultures (C2-2 vs. C2-1) with total DEPs-308; C2-2 high-107; C2-1 high-201 (Figure 7c). The identified top pathways include ECM-receptor interaction, ECM organization, beta catenin-independent Wnt pathway, regulation of apoptosis and cell cycle-related G1/S transition



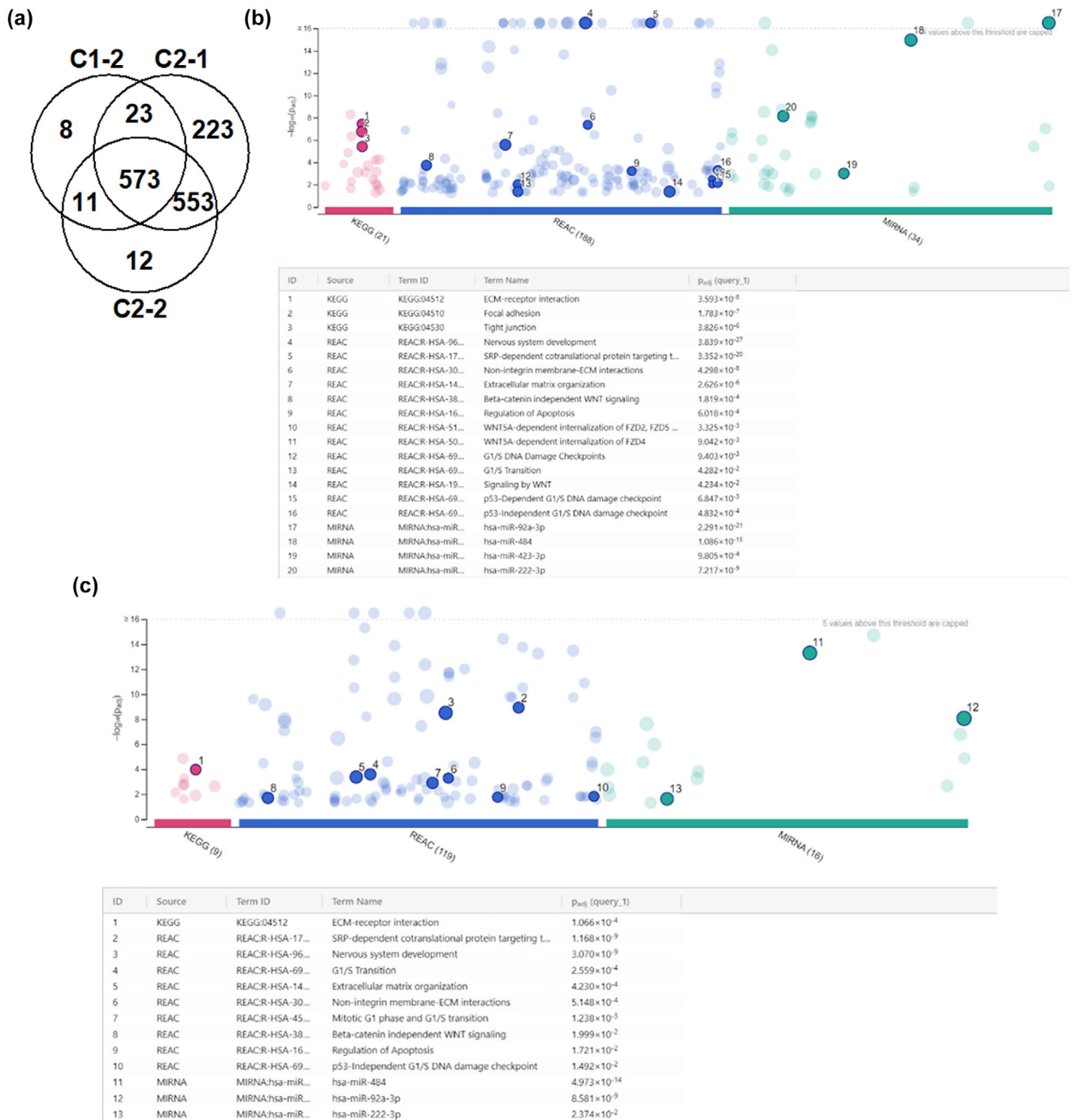


**FIGURE 7** Proteomics analysis of bioreactor-generated hiPSC-EV protein cargo. (a) Venn diagram of DEPs for the three EV groups (C1-2, C2-1 and C2-2); C1-1 group was not analysed due to the insufficient EV amount. GO annotation shows the pathway analysis of DEPs for (b) microcarrier versus aggregate in mTeSR (C2-2 vs. C1-2); total DEPs-502; C2-2 high-452; C1-2 high-50 and (c) different EV collect medium mTeSR versus HBM for microcarrier cultures (C2-2 vs. C2-1). Total DEPs-308; C2-2 high-107; C2-1 high-201. (d) Correlation of the DEPs in EVs with the DEGs in parent cells for microcarrier versus aggregate condition in mTeSR medium (C2-2 vs. C1-2). (e) GO analysis of top 400 proteins in hiPSC-EVs of C2-2 condition (microcarrier culture in mTeSR).

pathway. The predicted miR regulators versus miRs in EVs identified in previous literature (Bi et al., 2022) include miR-222-3p, 423-3p, 484 and 92a-3p (Figure S8). The specific protein cargo related to Wnt pathways is shown in Table S6 and the negative regulation of apoptosis-related proteins is shown in Table S7. For the correlation of the DEPs in the EVs with the DEGs in the parent cells, the overlapped DEGs and the DEPs were plotted against each other, indicating that the DEGs in the parent cells were also detected in the secreted EVs as DEPs (Figure 7d). The total overlapped number is 177, 115 of which were not plotted because the fold change in DEPs was 'INF', and the rest 62 are shown in the plot. A weak increasing trend for DEPs versus DEGs was observed, when comparing microcarrier with aggregate culture. As C2-2 condition is the most promising in generating

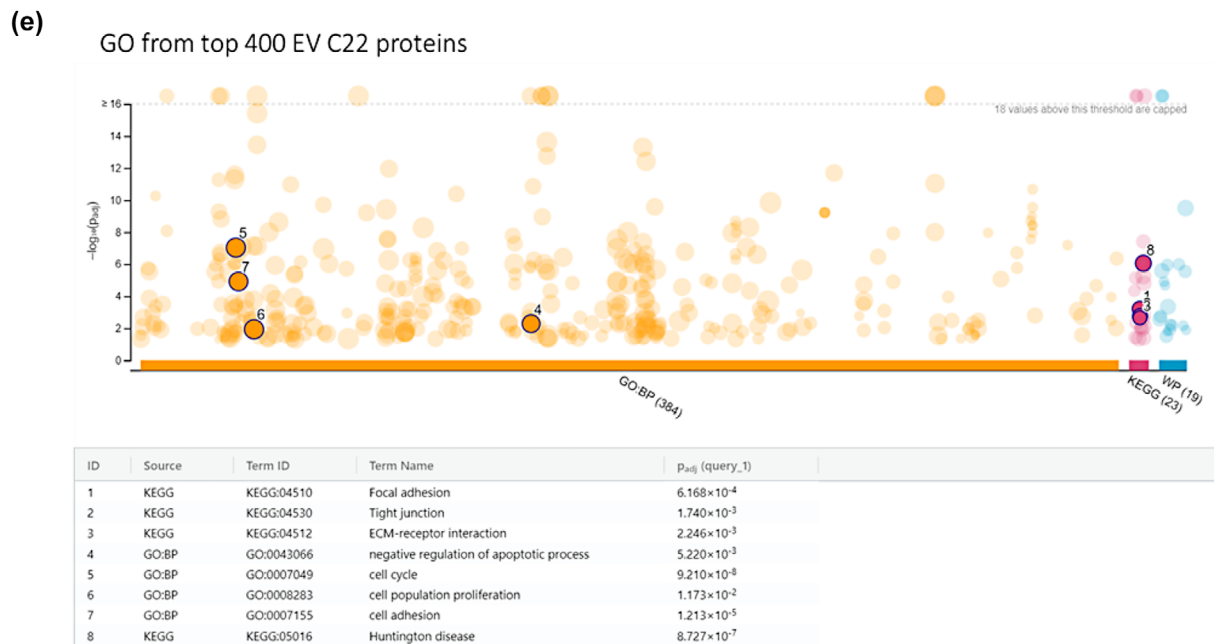
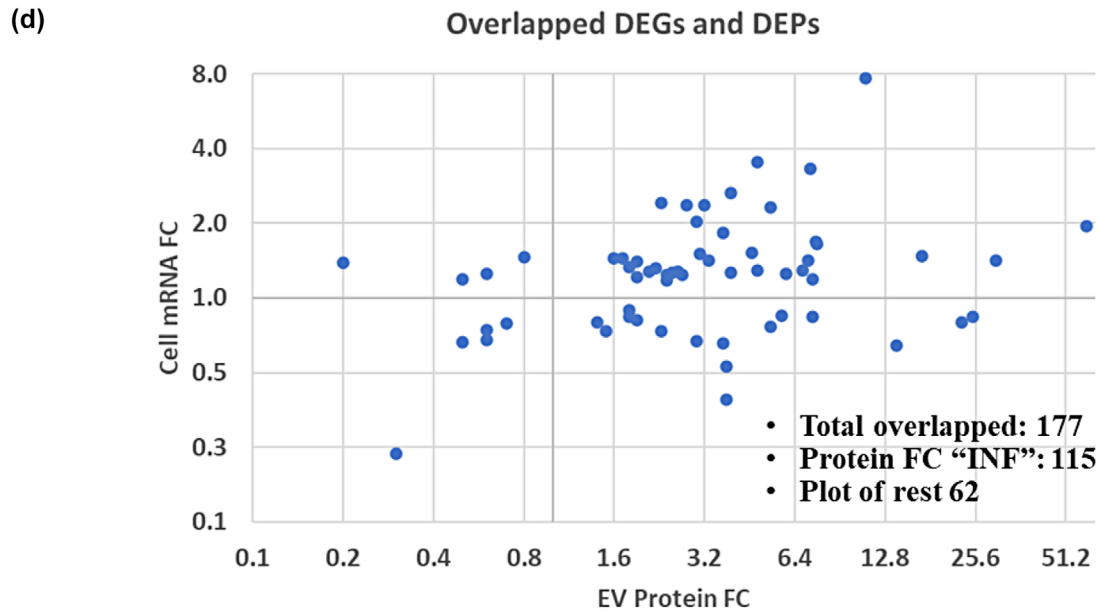


FIGURE 7 Continued

hiPSC-EVs, the top 400 proteins in C2-2 EVs were analysed by GO annotation (Figure 7e). The identified pathways for the C2-2 EV protein cargo include focal adhesion, tight junction, ECM-receptor interaction, negative regulation of apoptotic process, cell cycle, cell population proliferation, cell adhesion and Huntington disease. These results indicate that the protein cargo for the C2-2 EV condition is therapeutically relevant.

### 3.4 | EV miRNA cargo analysis by small RNA-sequencing

Since miRNA cargo contributes to a significant portion of the therapeutic effects of EVs, small RNA-seq was performed to analyse miRNA cargo in the EVs as well as the parent cells in order to understand the miRNA packaging (Figure 8, Excel Data File S4 and S5 and Tables 6 and 7). Only C2-1 and C2-2 conditions were evaluated as the C1-1 and C1-2 conditions did not have sufficient EVs. C2-2 EV had the highest yield and most therapeutically relevant protein cargo. For the four groups, the parent cells expressed a much larger number of miRNAs (~1200–1300) than the corresponding EVs (~500 for C2-1 and ~800 for the C2-2 group)

**TABLE 5** Negative regulation of apoptosis for C1-2 and C2-2 comparison (microcarrier vs. aggregate in mTeSR).

Identified proteins	Accession number	T-test (p-value)	Fold change	Quantitative profile
Asparagine synthetase	P08243	0.032	2.2	C1-2 low, C2-2 high
Endoplasmin	P14625	0.011	2.4	C1-2 low, C2-2 high
Receptor-type tyrosine-protein phosphatase zeta	P23471	0.00068	INF	C1-2 low, C2-2 high
60S ribosomal protein L10	P27635	0.0032	4.3	C1-2 low, C2-2 high
Cystathionine beta-synthase	P35520	0.00091	INF	C1-2 low, C2-2 high
Alanine-tRNA ligase, cytoplasmic	P49588	0.0008	8.4	C1-2 low, C2-2 high
Heterogeneous nuclear ribonucleoprotein K	P61978-3	< 0.00010	INF	C1-2 low, C2-2 high
26S proteasome regulatory subunit 4	P62191	0.047	INF	C1-2 low, C2-2 high
N-alpha-acetyltransferase 15, NatA auxiliary subunit	Q9BXJ9	<0.00010	INF	C1-2 low, C2-2 high
E2 ubiquitin-conjugating enzyme	Q9C0C9	<0.00010	INF	C1-2 low, C2-2 high

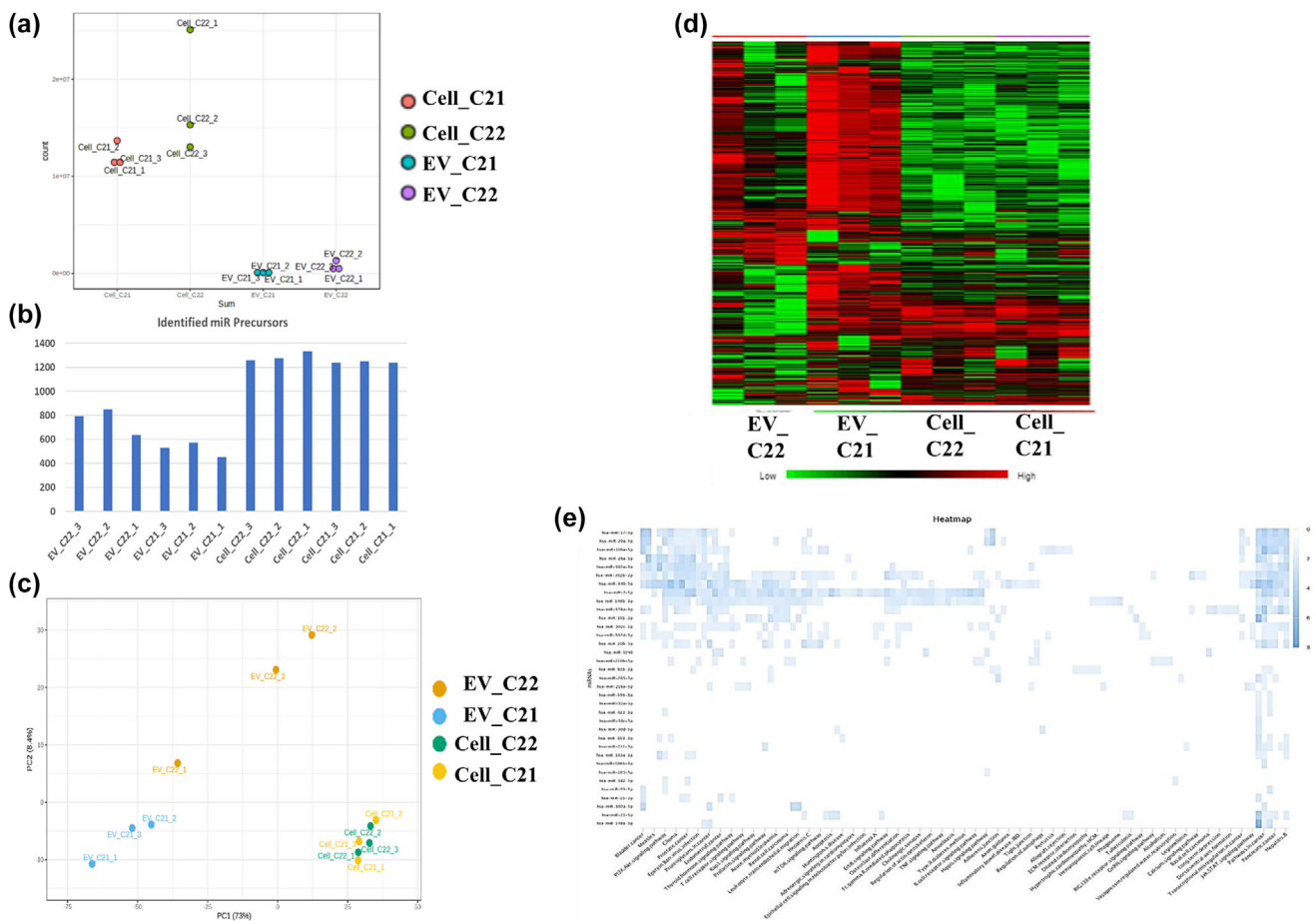


**FIGURE 8** miRNA-sequencing of hiPSC-EVs from VWBRs based on microcarrier cultures. (a) Total miRNA count for C2-1 (HBM) and C2-2 (mTeSR) conditions, including EVs and parent cells; (b) the number of identified miRs for each condition; (c) PCA plots to show the cluster of C2-1 and C2-2, EVs and cells; (d) heatmap illustration of top DEGs among the four conditions; (e) KEGG pathway analysis for the top 50 miRs of C2-2 EVs.

(Figure 8a,b). PCA plot showed the distinct clusters of the parent cells from the corresponding EVs (Figure 8c). The two cell conditions were closely clustered, while the two EV conditions were scattered and large variations among the three replicates were observed. Heatmap analysis further revealed the differences among the four conditions: C2-2 and C2-1 parent cells were more similar, and C2-2 and C2-1 EVs were more similar to each other (Figure 8d). The top 10 miRs in the EVs and the parent cells were shown in Table 6. For example, for C2-2 EVs, the most abundant mRNAs include miR-302a, 302b, 148a, 21, 20a, 302c, 302d, 182, 92a-1 and 92a-2. These 10 miRs were also identified in C2-1 EVs and the parent cells. For example, miR-302 may be

**TABLE 6** The top 10 miRs in the hiPSC-EVs and the parent cells (microcarrier culture).

EV_C2-2	EV_C2-1	Cell_C2-2	Cell_C2-1
hsa-mir-302a	hsa-mir-302a	hsa-mir-302a	hsa-mir-302b
hsa-mir-302b	hsa-mir-302b	hsa-mir-302b	hsa-mir-302a
hsa-mir-148a	hsa-mir-21	hsa-mir-21	hsa-mir-21
hsa-mir-21	hsa-mir-148a	hsa-mir-148a	hsa-mir-148a
hsa-mir-20a	hsa-mir-92a-1	hsa-mir-92a-1	hsa-mir-92a-1
hsa-mir-302d	hsa-mir-20a	hsa-mir-20a	hsa-mir-20a
hsa-mir-302c	hsa-mir-92a-2	hsa-mir-92a-2	hsa-mir-92a-2
hsa-mir-182	hsa-mir-302d	hsa-mir-302d	hsa-mir-302d
hsa-mir-92a-1	hsa-mir-302c	hsa-mir-302c	hsa-mir-302c
hsa-mir-92a-2	hsa-mir-182	hsa-mir-182	hsa-mir-182

**TABLE 7** The top miRs enriched in the specific tissue or cells by miTED analysis. Neural system or stem cell related tissue is highlighted.

hsa-miR-302a-5p	hsa-miR-148a-3p	hsa-miR-20a-5p	hsa-miR-17-5p
<b>Neural stem cells</b>	Bone marrow plasma cells	<b>Neural stem cells</b>	<b>Neural stem cells</b>
Testis	Hair follicle	CD4+ T cells	Bone marrow
<b>Induced pluripotent stem cells</b>	Jejunum	Epidermis	Foetal liver
Renal tubular cells	<b>Neural stem cells</b>	<b>Cerebellum</b>	Intrathoracic lymph nodes
miRXplore Universal Reference	Liver	<b>Umbilical cord</b>	Submandibular gland
Heart	Breastmilk	Salivary gland	Muscle
<b>Neuron</b>	Fundus uteri	<b>Adipose-derived stem cells</b>	Epidermis
Small intestine	Ligament	Foetal liver	Small intestine
Body of stomach	Lower-outer quadrant of breast	Lymph nodes of inguinal region or leg	<b>Cerebellum</b>
Subclavian artery	Rectosigmoid junction	<b>Spinal cord</b>	Lymph nodes of inguinal region or leg

related to pluripotency regulation, and highly expressed in neural stem cells, iPSCs, neurons and so forth (Table 7) (Li et al., 2016, 2016).

Volcano plot shows the 54 DEGs for microcarrier culture C2-2 versus C2-1 EVs, showing the effect of EV collection medium (Figure S11A). There were no DEGs for the parent cells of C2-2 versus C2-1 group, which indicates that the miRNA contents in the parent cells were almost the same. The top 10 miRNAs enriched in C2-2 versus C2-1 EVs include miR-1248, 8086, 5480, 619, 5480, 520 g, 495, 148a, 519d and 186. Other miRNAs enriched in the C2-2 group include miR-132, 133b, 302 and so forth (Excel Data file S4). For the C2-2 EV versus parent cells, there were 189 DEGs as shown in the volcano plot, showing the enriched miRNAs after EV packaging from the parent cells (Figure S11B). The top 10 miRNAs enriched in the C2-2 EV versus parent cells include miR-7704, 3976, 3182, 3665, 6516, 6883, 8086, 5588, 4508 and 4516. The KEGG pathway analysis was performed for the top 50 miRNAs for the C2-2 EVs (Figure 8e). These top 50 miRNAs were involved in PI3K-Akt signalling pathway, various cancers, T-cell receptor signalling pathway, Rap1, mTOR, ErbB signalling, regulation of actin cytoskeleton, tumour necrosis factor (TNF), B-cell receptor signalling, Hippo signalling, adherens junction, axon guidance, tight junction, regulation of autophagy, ECM-receptor interaction, hematopoietic cell lineage, phagosome, retinoic-acid inducible gene (RIG)1 like signalling, calcium signalling, dorsal-ventral axis formation, Jak-STAT signalling pathway and so forth. These results indicate that the miRNA cargo for the C2-2 EV condition is therapeutically relevant.

### 3.5 | hiPSC-EV functional assays *in vitro*

To test the function of hiPSC-EVs, an *in vitro* proliferation assay was performed on mouse microglia cell line BV2. Only C2-1 and C2-2 conditions were evaluated as the C1-1 and C1-2 conditions did not have sufficient EVs. Under equal amount of EV treatment, the proliferation of microglia was significantly inhibited by the EVs of C2-1 condition, while promoted by the EVs of



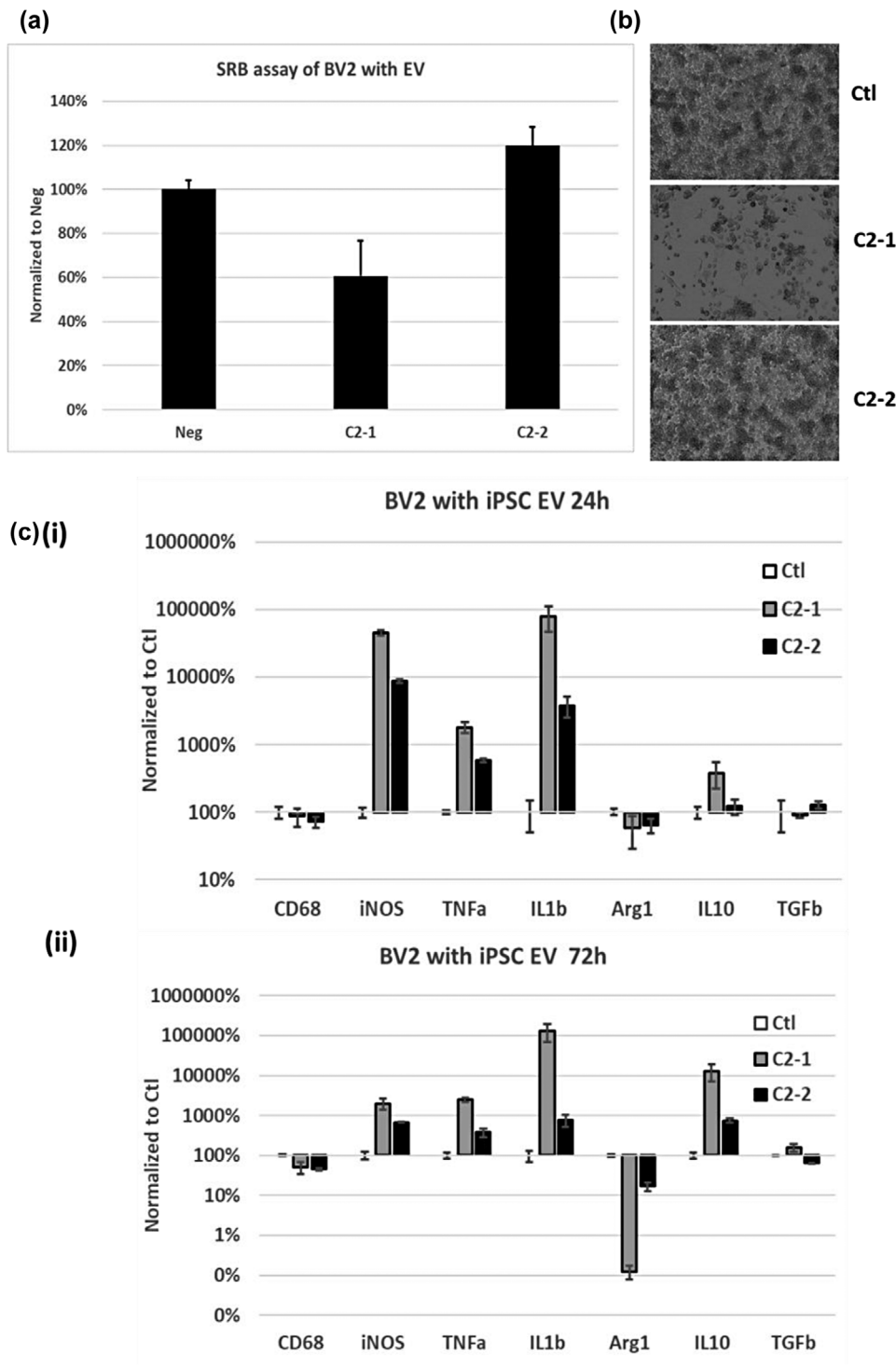


**FIGURE 9** BV2 microglia function analysis treated by hiPSC-EVs. (a) Sulforhodamine B (SRB) assay of BV2 cells treated with hiPSC-EVs for 3 days. Negative control indicates that the cells received no EV treatment. (b) Bright field image of treated BV2 cells at the end point of SRB assay. The control (Ctl) is the group that no EVs were added to the culture. (c) RT-qPCR assay of BV2 cells treated with hiPSC-EVs at 24 h (i) and 72 h (ii).  $n = 3$ . The two figures were plotted on the Log scale and all the samples were statistically significant from each other ( $p < 0.05$ ).

the C2-2 condition (Figure 9a,b). The inhibition or killing effect for C2-1 group may be from the M1 type cytokine and nitric oxide production. M1 macrophage is an end-stage killer cell that dies during the inflammatory response, possibly succumbing to its own NO production, as previously demonstrated *in vitro* (Albina et al., 1989). It may also be due to the contamination of cellular materials and/or apoptotic debris, as evidenced in the Western blot results for exosomal markers. In addition, the change of microglia morphology implies that C2-1 EVs induce M1 (pro-inflammatory) phenotype more than C2-2 EVs, as the cells appeared flattened-like ‘pancake’ shape compared to the M0 cells (Figure 9b). Pro-inflammatory genes related with M1 phenotype, such

as *iNOS*, *TNF- $\alpha$*  and *IL-1 $\beta$* , were downregulated for the C2-2 group compared to the C2-1 group after 24-h induction (Figure 9c), which suggests that C2-1 EVs induce M1 type activation of microglia. Those pro-inflammatory cytokines still showed very high induction levels after 72 h (Figure 9c). Expression of the anti-inflammatory gene *Arg-1* was almost completely absent in C2-1, but was much higher for the C2-2 group. Overall, these results indicate that the C2-2 EVs have less pro-inflammatory and more anti-inflammatory properties that can promote microglial proliferation.

## 4 | DISCUSSION

### 4.1 | Different 3-D hiPSC cultures reveal different metabolism

While hPSC expansion has been demonstrated on microcarriers or as aggregates in VWBRs (Borys et al., 2021; Nogueira et al., 2021; Rodrigues et al., 2018), no study has investigated the EV secretion of these two types of 3-D hPSC expansion systems and performed direct comparisons for EV cargo. This study also confirmed similar pluripotency, stemness and anti-senescence properties for hPSCs grown on microcarriers and as aggregates based on transcriptome analysis. VWBRs have been known as low shear stress (0.2–0.3 dyn/cm<sup>2</sup>) and suitable for human stem cell expansion (Table S8). Our previous study has compared hMSC-EV biomanufacturing in microcarrier-based VWBRs and showed 2–3 fold higher EVs (per million cells per day) for VWBRs than 2D culture and the agitation speed of 25–64 rpm resulted in similar EV secretion (Jeske et al., 2023). One step further, this study focuses on the comparison of microcarrier versus aggregate culture in terms of hiPSC-EV biomanufacturing.

Microcarrier cultures had 17–200 fold higher hiPSC-EVs (with small size) than the aggregate cultures for the three runs, independent of collection medium. This indicates that the microcarrier culture of hiPSCs has the enhanced ability to secrete EVs than aggregate culture. However, EV biogenesis markers did not show significant differences based on mRNA-seq and RT-qPCR only showed the increase for two out of nine markers. As most cells (>80%) in microcarrier culture were exposed to shear stress (Debbi et al., 2022) compared to aggregate culture (<50%), the EV shedding should be more significant for microcarrier culture. Metabolite analysis showed more glucose and glutamine metabolism for microcarrier cultures. Moreover, transcriptome analysis as well as RT-qPCR showed the different cellular metabolic processes for microcarrier culture compared to aggregate culture (C2-2 vs. C1-2), although cell expansion was similar, which may contribute to the increased EV secretion in microcarrier cultures. In particular, microcarrier cultures had higher expression of canonical glycolysis related-genes and lower autophagy-related genes than the aggregate cultures. VWBRs have 10-fold lower shear stress than stirred tank bioreactors or spinner flasks (Borys et al., 2021; Jeske et al., 2023, 2021), which may be beneficial for EV biogenesis in microcarrier cultures. In addition, the aggregation-induced integrated stress response (Bijonowski et al., 2020) and the possible nutrient diffusion limitation in the aggregate culture may expose the hiPSCs to more cellular stress than microcarrier culture.

Based on transcriptome analysis, the upregulated DEGs in microcarrier cultures were mainly involved in Wnt signalling, cell cycle, p53 signalling and ECM and actin cytoskeleton organization. Rap1 signalling, mTOR, MAPK, HIF-1 signalling, Hippo signalling and PI3K-Akt signalling were also identified. These pathways are consistent with those identified by EV proteomics analysis of protein cargo and miRNA-sequencing analysis of EV miRNA cargo. Microcarrier culture also had significantly higher expression of growth factor genes (*VEGFA*, *PDGFB*, *IGF2*, *noggin*, *EGF* etc.), and slightly higher expression of CDKs related to cell cycle. The ECM proteins such as collagens and laminins were also expressed at higher levels than aggregate culture. All these may contribute to hiPSC-EV secretion in microcarrier cultures.

Since the EV biogenesis markers of microcarrier and aggregate cultures in generally were similar (e.g. EV biogenesis markers were very different for VWBRs compared to 2D culture as shown in our previous study (Jeske et al., 2023)), one possibility is that aggregate cultures may contain many matrix-bound nanovesicles (Huleihel et al., 2016; Quijano et al., 2020), entrapped inside the aggregates within the ECM networks, and cannot be analysed through EV isolation from culture supernatants. Cell–matrix interactions were found to regulate the functional EV secretion from human stem cells and the elasticity of the ECM affects EV release and secretion (Lenzini et al., 2021, 2020). The intracellular CD63<sup>+</sup> multivesicular bodies transport faster in the human stem cells within the softer ECM microenvironment, leading to increased EV secretion, which could be sequestered by ECM networks. Therefore, isolation and characterization of these matrix-bound nanovesicles may be required.

### 4.2 | hiPSC-EV protein cargo analysis by proteomics

hiPSC-derived EV cargo has been compared to hESC-derived EVs and umbilical cord-derived hMSCs (Bi et al., 2022; Gupta et al., 2022). HiPSC-EVs and hESC-EVs had similar protein cargo in regulating development, metabolism and anti-aging effects, such as Wnt, cell cycle, AMPK and VEGF signalling pathways, while hMSC-EVs contributed more to immune regulation-related pathways, such as NF- $\kappa$ B, TNF and B receptor signalling (Bi et al., 2022; Gupta et al., 2022). The proteomics of EVs from hMSCs of bone marrow, adipose tissue and umbilical cord sources have been compared, indicating that the tissue origin could influence

EV protein cargo (Wang et al., 2020). In addition to human stem cell type and tissue origin, it has been recognized that the culture environment (3D vs. 2D, hypoxia, matrix elasticity and bioreactor hydrodynamics) also impacts protein cargo of the secreted EVs (Andrade et al., 2021; Jeske et al., 2023; Rocha et al., 2019; Yuan et al., 2022).

Compared to hPSC aggregate culture, microcarrier-based culture involves more cell–matrix interaction and cell adhesion. As such the top DEPs in C2-2 versus C2-1 are related to ECM–receptor interaction, focal adhesion, ECM organization and tight junction. In addition, the enriched pathways were related to G1/S transition (cell cycle), Wnt signalling (in particular Wnt5A), p53 signalling as well as regulation of apoptosis. Several identified miRNAs that regulate the DEPs include miR-92a, 484, 222 and 423. For the top 400 proteins in C2-2 EV cargo, they were mainly related to focal adhesion and cell adhesion, tight junction, ECM–receptor interaction, negative regulation of apoptotic process, cell cycle and proliferation, which may be reflected by the parent hiPSCs adhered to Synthamax II microcarriers and metabolic status of the expanded cells.

### 4.3 | hiPSC-EV miRNA cargo analysis by small RNA-seq

miRNAs of undifferentiated hiPSCs (e.g. through hiPSC secretome) should contribute significantly to the maintenance of stemness, as part role of the extracellular microenvironment (Baumann, 2021). When hiPSCs were induced for lineage-specific differentiations, such as lineages of hMSCs (Greca et al., 2018), cardiomyocytes (Louro et al., 2022) and neural stem cells (Hering & Shetty, 2023; Upadhyaya et al., 2020), the secreted EVs should acquire a stromal modulatory, or cardiac protective, or neuroprotective, neurogenic proteomic and miRNA pattern, respectively, during differentiation. In this study, miR-302 family was found to be abundant in the C2-2 and C2-1 EVs, which has been reported to regulate hPSC pluripotency and re-programming through Akt-Oct4, as well as attenuating amyloid-beta-induced neurotoxicity through activation of Akt signalling (Gao et al., 2022). Small RNA-seq also identified miR-21 in hiPSC-EVs, which has a variety of functions including regulation of mechanotransduction, neuroprotection, neurite outgrowth and modulation of proinflammatory microglia (Deng et al., 2022; Hurwitz et al., 2018; Vichai & Kirtikara, 2006; Xia et al., 2020). For other identified miRNAs in hiPSC-EVs, miR-148a can modulate immune responses by regulating inflammatory cytokines (Rebech et al., 2023). miR-20a may play anti-inflammatory and anti-apoptotic roles via deactivation of cytokine CXCL12 and CXC chemokine receptor (CXCR)4, NF- $\kappa$ B (nuclear factor kappa light chain enhancer of activated B cells) signalling and extracellular signal-regulated kinase (ERK)1/2 signalling (Zhang et al., 2020). It has been reported that transcription factor 7-like 2 (TCF7L2, T-cell specific) is the downstream of CXCR7/miR-182, and the Hippo/Yes-associated protein (YAP) pathway may be a key pathway in CXCR7 upregulation and plays a role in protecting the brain (Wang et al., 2023). miR-92a is also crucial for pluripotency regulation and can regulate MAPK1 and FoxO1 expression (Yu et al., 2023).

The top enriched miRNAs in C2-2 (i.e. microcarrier culture in mTeSR) EVs were linked to (1) the regulation of cell proliferation, metabolism and cell cycle, such as PI3K-Akt signalling pathway, Rap1, mTOR, ErbB signalling, Hippo signalling, regulation of autophagy and so forth, (2) immune modulation, such as T-cell receptor signalling pathway, TNF, B-cell receptor signalling, phagosome, Jak-STAT signalling pathway and RIGI-like signalling; (3) regulation of actin cytoskeleton, adherens junction, tight junction, ECM–receptor interaction, (4) differentiation and cellular function, such as hematopoietic cell lineage, calcium signalling, dorsal–ventral axis formation, axon guidance. In this study, the miRNA-seq detected a total of 800 miRNAs in the C2-2 EV condition (among of which there were 325 distinct miRNAs only expressed in this condition) and 500 miRNAs for the C2-1 condition, which are much more than that (only 18 miRNAs) reported in the literature (Figure S12) (Bi et al., 2022). The Venn diagram indicated that the miRNAs identified in the literature is a small subset of both C2-2 and C2-1 EVs. Understanding the role of each miRNA in the hiPSC-EVs requires further extensive investigation. The miRNAs in the EVs should be the subset of parent cell miRNAs, but were packaged into the EVs with upregulated or downregulated expression. The top miRNAs in volcano plot of C2-2 EVs versus cells were mostly large size (e.g. miR-3182, miR-8086), and their functions are poorly understood.

### 4.4 | Function of VWBR-biomanufactured hiPSC-EVs

One of the biggest advantages of hPSC-EVs is their rejuvenation or anti-senescence effects on the aged somatic cells or structure (such as blood–brain barrier). The anti-senescence effects of hPSC-EVs may be through transferring AKT1 and clathrin assembly lymphoid myeloid leukemia (CALM) proteins to activate the endothelial nitric oxide synthase (eNOS)–Sirt1 axis (Li et al., 2023), activating lysosomes (Hu et al., 2020), transferring SMADs to regulate the myelin transcription factor (MYT)1- egl-9 family hypoxia-inducible factor 3 (Egl3)-Sirt1 axis (Hu et al., 2021) or p38-MAPK signalling pathway (Liu et al., 2023). The senescent behaviour of bone marrow and adipose tissue-derived hMSCs have been investigated in our previous studies (Jeske et al., 2021; Yuan et al., 2020), and the Sirt1/3 family and nicotinamide adenine dinucleotide (NAD)/NAD<sup>+</sup>hydrogen (H) redox status play an important role in hMSC senescence. In this study, the transcriptome analysis showed a similar expression of Sirt1/3 for microcarrier versus aggregate culture, indicating that the EVs of both cultures should have anti-senescence effects. Rejuvenation of senescent hippocampal neural stem cells and alleviated age-related bone loss have also been observed for hPSC-EVs (Gong et al., 2020; Hu et al., 2020). hiPSC-derived mesenchymal stem cell-secreted EVs can enhance angiogenesis by inhibiting

Stat3-dependent autophagy (Xia et al., 2020). Our results showed the stimulated proliferation by C2-2 EVs, which could be the evidence of a rejuvenation effect.

Another benefit of hPSC-EVs is the immuno-modulation effects. Human stem cell-derived EVs have been shown to promote M2 microglial/macrophage polarization (Jiang et al., 2018). Regulatory T-cell modulation by embryonic stem cell-derived EVs has been reported (Xia et al., 2021). In this study, the C2-2 EVs also resulted in less M1 polarization of microglia and more M2 polarization compared to C2-1 EVs, showing the possible role of hiPSC-EVs in immuno-modulation. These functional outcomes could be due to the differential EV protein cargo and miRNA cargo profiles as well as the parent cell transcriptome. For example, intercellular adhesion molecules (ICAMs) mediate adhesive interactions for antigen-specific immune responses, lymphocyte recirculation and other cellular interactions important for immune responses (Bi et al., 2022). In addition, miR-132 can shift disease-associated (M1 type) to homeostatic microglia (Walgrave et al., 2023). In this study, the C2-2 condition had higher ICAMs and miR-132 than the C1-2 condition, which were consistent with the results of hiPSC-EV functional analysis using microglia. Additional functional analysis may be performed *in vitro* and *in vivo* in future studies.

#### 4.5 | Importance of EV collection medium

An important observation from this work is that the EV collection medium (during day 5–8) could affect the EV secretion as well as the protein and miRNA cargo. The mTeSR media used here is the standard hPSC expansion medium. HBM composition is chemically defined with serum-free components, which are fewer than mTeSR medium (Dang et al., 2021). Some of the differences in medium formulation can be revealed from metabolite analysis, especially for  $\text{Na}^+$ ,  $\text{K}^+$  and  $\text{Ca}^{2+}$  levels. mTeSR medium consistently resulted in 1.3–3 fold more EVs than HBM, independent of microcarrier or aggregate cultures. The effect of the culture medium of hPSCs is likely related to how the medium maintains the parent stem cell viability, proliferation and pluripotency. For example, it has been shown that 0.5% Knockout Serum Replacement is the optimal concentration for hiPSC culture, and that the culture supernatants can be continuously collected for 5 days for EV collection (Luo et al., 2021). These postulations were verified in the proteomics analysis of protein cargo of C2-2 versus C2-1 in this study, which shows the enriched pathways related to G1/S transition (cell cycle), Wnt signalling, p53 signalling, as well as regulation of apoptosis and ECM–receptor interaction.

In this study, while the same trends were observed for the four conditions among three different runs, large variations in the produced EVs and expanded cell numbers and so forth were observed from run to run. This is in large part due to the identification of operational parameters especially in Run 1 for the operator, as no prior training was performed before the experiments at the PBS Biotech. Run 2 and Run 3 were closer in the bioreactor performance with higher EV yields. After the three runs, the standard operational procedure was finalized and smaller variations would be expected. This study used 100-mL VWBRs and in principle the process can be scaled up to 500 mL, 3 L and up to 80 L for large-scale hiPSC-EV production. Our previous study using this bioreactor system for the generation of hMSC-derived EVs shows that this system is reproducible and scalable (from 0.1 to 0.5 L) (Jeske et al., 2023). In addition, the effect of shear stress on the production of large EVs may cause a large size distribution of EVs (Thompson & Papoutsakis, 2023; Thone & Kwon, 2020). It is postulated that this effect is related to the shear stress levels exerted on the cells. The low shear stress levels (0.1–0.3  $\text{dyn}/\text{cm}^2$ ) in VWBRs are more physiologically relevant than the stirred tank bioreactors, which should have minimal influence on the production of large EVs.

## 5 | CONCLUSIONS

This study identified that the microcarrier-based expansion of undifferentiated hiPSCs in mTeSR medium robustly generated the most EVs with high quantity and quality compared to other conditions based on nanoparticle tracking analysis (for EV size and yield), EV proteomics and small RNA-sequencing for EV miRNA cargo. The more glycolytic metabolic pathways confirmed by transcriptome analysis of hiPSCs, and the higher percentage of cells exposure to shear stress in microcarrier culture may contribute to the promoted EV secretion. On the other hand, the EV penetration in tissue-like environments and matrix-bound nanovesicles may be worth investigating for aggregate cultures. To our knowledge, this is the first study to report a systematic and comprehensive analysis of protein cargo by proteomics and miRNA profiles of EVs secreted by hiPSCs expanded on microcarriers or as aggregate in a dynamic VWBR. This study provides a scalable biomanufacturing platform with defined cargo profiles for hPSC-EV production for the applications in drug development and cell-free therapeutics in pre-clinical or clinical settings.

### AUTHOR CONTRIBUTIONS

**Laureana Muok:** Data curation (equal); formal analysis (equal); investigation (equal); methodology (equal); visualization (equal); writing—original draft (equal). **Li Sun:** Conceptualization (supporting); data curation (equal); formal analysis (equal); investigation (equal); methodology (equal); software (equal); validation (supporting); visualization (equal); writing—review and editing (equal). **Colin Esmonde:** Data curation (supporting); investigation (supporting); methodology (supporting); validation (supporting). **Hannah Worden:** Data curation (supporting); investigation (supporting); methodology (supporting); validation



(supporting). **Cynthia Vied**: Formal analysis (supporting); investigation (supporting); methodology (supporting); software (supporting). **Leanne Duke**: Data curation (supporting); investigation (supporting); methodology (supporting). **Shaoyang Ma**: Formal analysis (supporting); investigation (supporting); methodology (supporting). **Olivia Zeng**: Formal analysis (supporting); investigation (supporting); methodology (supporting). **Tristan Driscoll**: Investigation (supporting); methodology (supporting); supervision (supporting); writing—review and editing (supporting). **Sunghoon Jung**: Conceptualization (supporting); data curation (supporting); funding acquisition (supporting); investigation (supporting); methodology (supporting); project administration (supporting); supervision (supporting). **Yan Li**: Conceptualization (lead); data curation (equal); funding acquisition (lead); investigation (equal); methodology (equal); project administration (lead); resources (lead); supervision (lead); visualization (equal); writing—original draft (equal); writing—review and editing (lead).

## ACKNOWLEDGEMENTS

The authors would thank for the support by FSU College of Medicine Translational Science laboratory for proteomics, mRNA-seq and miRNA-Seq, Dr Brian K. Washburn at FSU Department of Biological Sciences for his help with RT-PCR analysis. L.M. held McKnight Doctorial Fellowship and was also supported in part by FAMU Title III funding. This work is supported by the National Science Foundation CAREER award (CBET-1652992 and CBET-1917618). The Hitachi HT7800 for TEM was funded from NSF Grant 2017869. Research reported in this publication was also partially supported by the National Institutes of Health (USA) under Award Number R01NS125016. The content is solely the responsibility of the authors and does not necessarily represent the official views of the National Institutes of Health.

## CONFLICT OF INTEREST STATEMENT

The authors declare no conflicts of interest.

## DATA AVAILABILITY STATEMENT

The datasets generated during and/or analysed during the current study are available from the corresponding authors on reasonable request.

## ORCID

Li Sun  <https://orcid.org/0000-0001-8228-7487>

Yan Li  <https://orcid.org/0000-0002-5938-8519>

## REFERENCES

- Adamiak, M., Cheng, G., Bobis-Wozowicz, S., Zhao, L., Kedracka-Krok, S., Samanta, A., Karnas, E., Xuan, Y. T., Skupien-Rabian, B., Chen, X., Jankowska, U., Girgis, M., Sekula, M., Davani, A., Lasota, S., Vincent, R. J., Sarna, M., Newell, K. L., Wang, O. L., ... Zuba-Surma, E. K. (2018). Induced pluripotent stem cell (iPSC)-derived extracellular vesicles are safer and more effective for cardiac repair than iPSCs. *Circulation Research*, *122*(2), 296–309.
- Albina, J. E., Caldwell, M. D., Henry, W. L., Jr., & Mills, C. D. (1989). Regulation of macrophage functions by L-arginine. *Journal of Experimental Medicine*, *169*(3), 1021–1029.
- Andrade, A. C., Wolf, M., Binder, H. M., Gomes, F. G., Manstein, F., Ebner-Peking, P., Poupardin, R., Zweigerdt, R., Schallmoser, K., & Strunk, D. (2021). Hypoxic conditions promote the angiogenic potential of human induced pluripotent stem cell-derived extracellular vesicles. *International Journal of Molecular Sciences*, *22*(8), 3890.
- Arthur, P., Kandoi, S., Sun, L., Kalvala, A., Kutehria, S., Bhattacharya, S., Kulkarni, T., Nimma, R., Li, Y., Lamba, D. A., & Singh, M. (2023). Biophysical, molecular and proteomic profiling of human retinal organoids derived exosomes. *Pharmaceutical Research*, *40*(4), 801–816.
- Baghbaderani, B. A., Tian, X., Neo, B. H., Burkall, A., Dimezzo, T., Sierra, G., Zeng, X., Warren, K., Kovarcik, D. P., Fellner, T., & Rao, M. S. (2015). cGMP-manufactured human induced pluripotent stem cells are available for pre-clinical and clinical applications. *Stem Cell Reports*, *5*(4), 647–659.
- Baumann, K. (2021). EVs promote stemness. *Nature Reviews Molecular Cell Biology*, *22*(2), 72–73.
- Bi, Y., Qiao, X., Liu, Q., Song, S., Zhu, K., Qiu, X., Zhang, X., Jia, C., Wang, H., Yang, Z., Zhang, Y., & Ji, G. (2022). Systemic proteomics and miRNA profile analysis of exosomes derived from human pluripotent stem cells. *Stem Cell Research & Therapy*, *13*(1), 449.
- Bijonowski, B. M., Fu, Q., Yuan, X., Irianto, J., Li, Y., Grant, S. C., & Ma, T. (2020). Aggregation-induced integrated stress response rejuvenates stemness of culture-expanded human mesenchymal stem cells. *Biotechnology and Bioengineering*, *117*, 3136–3149.
- Borys, B. S., Dang, T., So, T., Rohani, L., Revay, T., Walsh, T., Thompson, M., Argiropoulos, B., Rancourt, D. E., Jung, S., Hashimura, Y., Lee, B., & Kallos, M. S. (2021). Overcoming bioprocess bottlenecks in the large-scale expansion of high-quality hiPSC aggregates in vertical-wheel stirred suspension bioreactors. *Stem Cell Res Ther*, *12*(1), 55.
- Borys, B. S., So, T., Colter, J., Dang, T., Roberts, E. L., Revay, T., Larijani, L., Krawetz, R., Lewis, I., Argiropoulos, B., Rancourt, D. E., Jung, S., Hashimura, Y., Lee, B., & Kallos, M. S. (2020). Optimized serial expansion of human induced pluripotent stem cells using low-density inoculation to generate clinically relevant quantities in vertical-wheel bioreactors. *Stem Cells Translational Medicine*, *9*(9), 1036–1052.
- Cone, A. S., Yuan, X., Sun, L., Duke, L. C., Vreones, M. P., Carrier, A. N., Kenyon, S. M., Carver, S. R., Benthem, S. D., Stimmell, A. C., Moseley, S. C., Hike, D., Grant, S. C., Wilber, A. A., Olcese, J. M., & Meckes, D. G. J. (2021). Mesenchymal stem cell-derived extracellular vesicles ameliorate Alzheimer's disease-like phenotypes in a preclinical mouse model. *Theranostics*, *11*(17), 8129–8142.
- Cuesta-Gomez, N., Verhoeff, K., Dadheech, N., Dang, T., Jasra, I. T., de Leon, M. B., Pawlick, R., Marfil-Garza, B., Anwar, P., Razavy, H., Zapata-Morin, P. A., Jickling, G., Thiesen, A., O'Gorman, D., Kallos, M. S., & Shapiro, A. M. J. (2023). Suspension culture improves iPSC expansion and pluripotency phenotype. *Stem Cell Research & Therapy*, *14*(1), 154.



- Dang, T., Borys, B. S., Kanwar, S., Colter, J., Worden, H., Blatchford, A., Croughan, M. S., Hossan, T., Rancourt, D. E., Lee, B., Kallos, M. S., & Jung, S. (2021). Computational fluid dynamic characterization of vertical-wheel bioreactors used for effective scale-up of human induced pluripotent stem cell aggregate culture. *The Canadian Journal of Chemical Engineering*, 99(11), 2536–2553.
- de Almeida Fuzeta, M., Bernardes, N., Oliveira, F. D., Costa, A. C., Fernandes-Platzgummer, A., Farinha, J. P., Rodrigues, C. A. V., Jung, S., Tseng, R. J., Milligan, W., Lee, B., Castanho, M., Gaspar, D., Cabral, J. M. S., & da Silva, C. L. (2020). Scalable production of human mesenchymal stromal cell-derived extracellular vesicles under serum-/xeno-free conditions in a microcarrier-based bioreactor culture system. *Frontiers in Cell and Developmental Biology*, 8, 553444.
- Debbi, L., Guo, S., Safina, D., & Levenberg, S. (2022). Boosting extracellular vesicle secretion. *Biotechnology Advances*, 59, 107983.
- Deng, P., Wang, L., Zhang, Q., Chen, S., Zhang, Y., Xu, H., Chen, H., Xu, Y., He, W., Zhang, J., & Sun, H. (2022). Therapeutic potential of a combination of electroacupuncture and human iPSC-derived small extracellular vesicles for ischemic stroke. *Cells*, 11(5), 820.
- Dougherty, J. A., Kumar, N., Noor, M., Angelos, M. G., Khan, M., Chen, C. A., & Khan, M. (2018). Extracellular vesicles released by human induced-pluripotent stem cell-derived cardiomyocytes promote angiogenesis. *Frontiers in Physiology*, 9, 1794.
- Gao, R., Ye, T., Zhu, Z., Li, Q., Zhang, J., Yuan, J., Zhao, B., Xie, Z., & Wang, Y. (2022). Small extracellular vesicles from iPSC-derived mesenchymal stem cells ameliorate tendinopathy pain by inhibiting mast cell activation. *Nanomedicine (Lond)*, 17(8), 513–529.
- Gong, L., Chen, B., Zhang, J., Sun, Y., Yuan, J., Niu, X., Hu, G., Chen, Y., Xie, Z., Deng, Z., Li, Q., & Wang, Y. (2020). Human ESC-sEVs alleviate age-related bone loss by rejuvenating senescent bone marrow-derived mesenchymal stem cells. *Journal of Extracellular Vesicles*, 9(1), 1800971.
- Greca, A. L. a., Solari, C., Furmento, V., Lombardi, A., Biani, M. C., Aban, C., Moro, L., Garcia, M., Guberman, A. S., Sevlever, G. E., Miriuka, S. G., & Luzzani, C. (2018). Extracellular vesicles from pluripotent stem cell-derived mesenchymal stem cells acquire a stromal modulatory proteomic pattern during differentiation. *Experimental & Molecular Medicine*, 50(9), 119.
- Gu, Z., Yin, Z., Song, P., Wu, Y., He, Y., Zhu, M., Wu, Z., Zhao, S., Huang, H., Wang, H., Tong, C., & Qi, Z. (2022). Safety and biodistribution of exosomes derived from human induced pluripotent stem cells. *Frontiers in Bioengineering and Biotechnology*, 10, 949724.
- Gupta, S., Krishnakumar, V., Soni, N., Rao, E. P., Banerjee, A., & Mohanty, S. (2022). Comparative proteomic profiling of Small Extracellular vesicles derived from iPSCs and tissue specific mesenchymal stem cells. *Experimental Cell Research*, 420(2), 113354.
- Hering, C., & Shetty, A. K. (2023). Extracellular vesicles derived from neural stem cells, astrocytes, and microglia as therapeutics for easing TBI-induced brain dysfunction. *Stem Cells Translational Medicine*, 12, 140–153.
- Hu, G., Xia, Y., Chen, B., Zhang, J., Gong, L., Chen, Y., Li, Q., Wang, Y., & Deng, Z. (2021). ESC-sEVs rejuvenate aging hippocampal NSCs by transferring SMADs to regulate the MYT1-Egln3-Sirt1 axis. *Molecular Therapy*, 29(1), 103–120.
- Hu, G., Xia, Y., Zhang, J., Chen, Y., Yuan, J., Niu, X., Zhao, B., Li, Q., Wang, Y., & Deng, Z. (2020). ESC-sEVs rejuvenate senescent hippocampal NSCs by activating lysosomes to improve cognitive dysfunction in vascular dementia. *Advanced Science (Weinh)*, 7(10), 1903330.
- Hua, T., Liu, C., Kiran, S., Gray, K. M., Jung, S., Meckes, D. G. J., Li, Y., & Sang, Q. A. (2022). Phenotypic, metabolic, and biogenesis properties of human stem cell-derived cerebellar spheroids. *Scientific Reports*, 12, 12880.
- Huleihel, L., Hussey, G. S., Naranjo, J. D., Zhang, L., Dziki, J. L., Turner, N. J., Stolz, D. B., & Badylak, S. F. (2016). Matrix-bound nanovesicles within ECM bioscaffolds. *Science Advances*, 2(6), e1600502.
- Hurwitz, S. N., & Meckes, D. G., Jr. (2017). An adaptable polyethylene glycol-based workflow for proteomic analysis of extracellular vesicles. *Methods in Molecular Biology*, 1660, 303–317.
- Hurwitz, S. N., Sun, L., Cole, K. Y., Ford, C. R., 3rd, Olcese, J. M., & Meckes, D. G., Jr. (2018). An optimized method for enrichment of whole brain-derived extracellular vesicles reveals insight into neurodegenerative processes in a mouse model of Alzheimer's disease. *Journal of Neuroscience Methods*, 307, 210–220.
- Jeske, R., Bejoy, J., Marzano, M., & Li, Y. (2020). Human induced pluripotent stem cell-derived extracellular vesicles: Characteristics and applications. *Tissue Engineering Part B Reviews*, 26(2), 129–144.
- Jeske, R., Chen, X., Ma, S., Zeng, E. Z., Driscoll, T. P., & Li, Y. (2022). Bioreactor expansion reconfigures metabolism and extracellular vesicle biogenesis of human adipose-derived stem cells in vitro. *Biochemical Engineering Journal*, 188, 108711.
- Jeske, R., Chen, X., Mulderrig, L., Liu, C., Cheng, W., Zeng, O. Z., Zeng, C., Guan, J., Hallinan, D., Yuan, X., & Li, Y. (2022). Engineering human mesenchymal bodies in a novel 3-D printed microchannel bioreactor for studying extracellular vesicle biogenesis. *Bioengineering (Basel)*, 9(12), 795.
- Jeske, R., Lewis, S., Tsai, A. C., Sanders, K., Liu, C., Yuan, X., & Li, Y. (2021). Agitation in a microcarrier-based spinner bioreactor modulates homeostasis of human mesenchymal stem cells. *Biochemical Engineering Journal*, 168, 107947.
- Jeske, R., Liu, C., Duke, L., Canonicco Castro, M. L., Muok, L., Arthur, P., Singh, M., Sung, L., Sun, L., & Li, Y. (2023). Upscaling human mesenchymal stem cell production in a novel vertical wheel bioreactor enhances extracellular vesicle secretion and cargo profile. *Bioactive Materials*, 25, 732–747.
- Jeske, R., Yuan, X., Fu, Q., Bunnell, B., Logan, T. M., & Li, Y. (2021). In vitro culture expansion shifts the immune phenotype of human adipose-derived mesenchymal stem cells. *Front Immunol*, 12, 621744.
- Jiang, M., Wang, H., Jin, M., Yang, X., Ji, H., Jiang, Y., Zhang, H., Wu, F., Wu, G., Lai, X., Cai, L., Hu, R., Xu, L., & Li, L. (2018). Exosomes from MiR-30d-5p-ADSCs reverse acute ischemic stroke-induced, autophagy-mediated brain injury by promoting M2 microglial/macrophage polarization. *Cellular Physiology and Biochemistry*, 47(2), 864–878.
- Karnas, E., Sekula-Stryjewska, M., Kmiotek-Wasyłewska, K., Bobis-Wozowicz, S., Ryszawy, D., Sarna, M., Madeja, Z., & Zuba-Surma, E. K. (2021). Extracellular vesicles from human iPSCs enhance reconstitution capacity of cord blood-derived hematopoietic stem and progenitor cells. *Leukemia*, 35(10), 2964–2977.
- Lasser, C., Eldh, M., & Lotvall, J. (2012). Isolation and characterization of RNA-containing exosomes. *Journal of Visualized Experiments: JoVE*, (59), e3037. <https://doi.org/10.3791/3037>
- Lembong, J., Kirian, R., Takacs, J. D., Olsen, T. R., Lock, L. T., Rowley, J. A., & Ahsan, T. (2020). Bioreactor parameters for microcarrier-based human MSC expansion under xeno-free conditions in a vertical-wheel system. *Bioengineering (Basel)*, 7(3), 73.
- Lenzini, S., Bargi, R., Chung, G., & Shin, J. W. (2020). Matrix mechanics and water permeation regulate extracellular vesicle transport. *Nature Nanotechnology*, 15(3), 217–223.
- Lenzini, S., Debnath, K., Joshi, J. C., Wong, S. W., Srivastava, K., Geng, X., Cho, I. S., Song, A., Bargi, R., Lee, J. C., Mo, G. C. H., Mehta, D., & Shin, J. W. (2021). Cell-matrix interactions regulate functional extracellular vesicle secretion from mesenchymal stromal cells. *ACS Nano*, 15(11), 17439–17452.
- Li, H. H., Lin, S. L., Huang, C. N., Lu, F. J., Chiu, P. Y., Huang, W. N., Lai, T. J., & Lin, C. L. (2016). miR-302 attenuates amyloid-beta-induced neurotoxicity through activation of Akt signaling. *Journal of Alzheimer's Disease*, 50(4), 1083–1098.
- Li, H. L., Wei, J. F., Fan, L. Y., Wang, S. H., Zhu, L., Li, T. P., Lin, G., Sun, Y., Sun, Z. J., Ding, J., Liang, X. L., Li, J., Han, Q., & Zhao, R. C. (2016). miR-302 regulates pluripotency, teratoma formation and differentiation in stem cells via an AKT1/OCT4-dependent manner. *Cell Death & Disease*, 7(1), e2078.
- Li, Q., Niu, X., Yi, Y., Chen, Y., Yuan, J., Zhang, J., Li, H., Xia, Y., Wang, Y., & Deng, Z. (2023). Inducible pluripotent stem cell-derived small extracellular vesicles rejuvenate senescent blood-brain barrier to protect against ischemic stroke in aged mice. *ACS Nano*, 17(1), 775–789.

- Liu, B., Lee, B. W., Nakanishi, K., Villasante, A., Williamson, R., Metz, J., Kim, J., Kanai, M., Bi, L., Brown, K., Di Paolo, G., Homma, S., Sims, P. A., Topkara, V. K., & Vunjak-Novakovic, G. (2018). Cardiac recovery via extended cell-free delivery of extracellular vesicles secreted by cardiomyocytes derived from induced pluripotent stem cells. *Nature Biomedical Engineering*, 2(5), 293–303.
- Liu, C., Helsper, S., Marzano, M., Chen, X., Muok, L., Esmonde, C., Zeng, C., Sun, L., Grant, S. C., & Li, Y. (2022). Human forebrain organoid-derived extracellular vesicle labelling with iron oxides for in vitro magnetic resonance imaging. *Biomedicines*, 10(12), 3060.
- Liu, C., & Su, C. (2019). Design strategies and application progress of therapeutic exosomes. *Theranostics*, 9(4), 1015–1028.
- Liu, P., Ewald, J., Pang, Z., Legrand, E., Jeon, Y. S., Sangiovanni, J., Hacariz, O., Zhou, G., Head, J. A., Basu, N., & Xia, J. (2023). ExpressAnalyst: A unified platform for RNA-sequencing analysis in non-model species. *Nature Communications*, 14(1). <https://doi.org/10.1038/s41467-023-38785-y>
- Liu, S., Mahairaki, V., Bai, H., Ding, Z., Li, J., Witwer, K. W., & Cheng, L. (2019). Highly purified human extracellular vesicles produced by stem cells alleviate aging cellular phenotypes of senescent human cells. *Stem Cells*, 37(6), 779–790.
- Liu, Y., Gu, S., Su, Y., Wang, S., Cheng, Y., Sang, X., Jin, L., Liu, Y., Li, C., Liu, W., Chen, M., Wang, X., & Wang, Z. (2023). Embryonic stem cell extracellular vesicles reverse the senescence of retinal pigment epithelial cells by the p38MAPK pathway. *Experimental Eye Research*, 227, 109365.
- Louro, A. F., Paiva, M. A., Oliveira, M. R., Kasper, K. A., Alves, P. M., Gomes-Alves, P., & Serra, M. (2022). Bioactivity and miRNome profiling of native extracellular vesicles in human induced pluripotent stem cell-cardiomyocyte differentiation. *Advanced Science (Weinh)*, 9(15), e2104296.
- Ludwig, T. E., Levenstein, M. E., Jones, J. M., Berggren, W. T., Mitchen, E. R., Frane, J. L., Crandall, L. J., Daigh, C. A., Conard, K. R., Piekarczyk, M. S., Llanas, R. A., & Thomson, J. A. (2006). Derivation of human embryonic stem cells in defined conditions. *Nature Biotechnology*, 24(2), 185–187.
- Luo, Y., Gao, D., Wang, P., Lou, C., Li, T., Niu, W., & Gao, Y. (2021). Optimized culture methods for isolating small extracellular vesicles derived from human induced pluripotent stem cells. *Journal of Extracellular Vesicles*, 10(6), e12065.
- Marzano, M., Bejoy, J., Cheerathodi, M., Sun, L., York, S., Zhao, J., Kanekiyo, T., Bu, G., Meckes, D. G., Jr., & Li, Y. (2019). Differential effects of extracellular vesicles of lineage-specific human pluripotent stem cells on cellular behaviours of isogenic cortical spheroids. *Cells*, 8, 993–1014.
- Marzano, M., Bou-Dargham, M. J., Cone, A. S., York, S., Helsper, S., Grant, S. C., Meckes, D. G., Jr., Sang, Q. X., & Li, Y. (2021). Biogenesis of extracellular vesicles produced from human stem cell-derived cortical spheroids exposed to iron oxides. *ACS Biomaterials Science & Engineering*, 7(3), 1111–1122.
- Muok, L., Liu, C., Chen, X., Esmonde, C., Arthur, P., Wang, X., Singh, M., Driscoll, T. P., & Li, Y. (2023). Inflammatory response and exosome biogenesis of choroid plexus organoids derived from human pluripotent stem cells. *International Journal of Molecular Sciences*, 24(8), 7660.
- Nogueira, D. E. S., Rodrigues, C. A. V., Hashimura, Y., Jung, S., Lee, B., & Cabral, J. M. S. (2021). Suspension culture of human induced pluripotent stem cells in single-use vertical-wheel bioreactors using aggregate and microcarrier culture systems. *Methods in Molecular Biology*, 2286, 167–178.
- Patel, D. B., Santoro, M., Born, L. J., Fisher, J. P., & Jay, S. M. (2018). Towards rationally designed biomanufacturing of therapeutic extracellular vesicles: Impact of the bioproduction microenvironment. *Biotechnology Advances*, 36(8), 2051–2059.
- Quijano, L. M., Naranjo, J. D., El-Mossier, S., Turner, N. J., Molina, C. P., Bartolacci, J., Zhang, L., White, L., Li, H., & Badylak, S. F. (2020). Matrix-bound nanovesicles: The effects of isolation method upon yield, purity and function. *Tissue Engineering Part C Methods*, 26, 528–540.
- Rebech, G. T., Bragato, J. P., Costa, S. F., de Freitas, J. H., Dos Santos, M. O., Soares, M. F., Eugenio, F. R., Dos Santos, P. S. P., & de Lima, V. M. F. (2023). miR-148a regulation interferes in inflammatory cytokine and parasitic load in canine leishmaniasis. *PLoS Neglected Tropical Diseases*, 17(1), e0011039.
- Rider, M. A., Hurwitz, S. N., & Meckes, D. G., Jr. (2016). ExtraPEG: A polyethylene glycol-based method for enrichment of extracellular vesicles. *Scientific Reports*, 6, 23978.
- Rocha, S., Carvalho, J., Oliveira, P., Voglstaetter, M., Schwartz, D., Thomsen, A. R., Walter, N., Khanduri, R., Sanchez, J. C., Keller, A., Oliveira, C., & Nazarenko, I. (2019). 3D cellular architecture affects microRNA and protein cargo of extracellular vesicles. *Advanced Science (Weinh)*, 6(4), 1800948.
- Rodrigues, C. A., Silva, T. P., Nogueira, D. E., Fernandes, T. G., Hashimura, Y., Wesselschmidt, R., Diogo, M. M., Lee, B., & Cabral, J. M. (2018). Scalable culture of human induced pluripotent cells on microcarriers under xeno-free conditions using single-use vertical-wheel™ bioreactors. *Journal of Chemical Technology & Biotechnology*, 93(12), 3597–3606.
- Silva, T. P., Fernandes, T. G., Nogueira, D. E. S., Rodrigues, C. A. V., Bekman, E. P., Hashimura, Y., Jung, S., Lee, B., Carmo-Fonseca, M., & Cabral, J. M. S. (2020). Scalable generation of mature cerebellar organoids from human pluripotent stem cells and characterization by immunostaining. *Journal of Visualized Experiments: JoVE*, 00(160). doi:10.3791/61143
- Silva, T. P., Sousa-Luis, R., Fernandes, T. G., Bekman, E. P., Rodrigues, C. A. V., Vaz, S. H., Moreira, L. M., Hashimura, Y., Jung, S., Lee, B., Carmo-Fonseca, M., & Cabral, J. M. S. (2021). Transcriptome profiling of human pluripotent stem cell-derived cerebellar organoids reveals faster commitment under dynamic conditions. *Biotechnology and Bioengineering*, 18(7), 2781–2803.
- Song, L., Wang, K., Li, Y., & Yang, Y. (2016). Nanotopography promoted neuronal differentiation of human induced pluripotent stem cells. *Colloids and Surfaces B: Biointerfaces*, 148, 49–58.
- Taheri, B., Soleimani, M., Fekri Aval, S., Esmaeili, E., Bazi, Z., & Zarghami, N. (2018). Induced pluripotent stem cell-derived extracellular vesicles: A novel approach for cell-free regenerative medicine. *Journal of Cellular Physiology*, 234(6), 8455–8464.
- Thompson, W., & Papoutsakis, E. T. (2023). The role of biomechanical stress in extracellular vesicle formation, composition and activity. *Biotechnology Advances*, 66, 108158.
- Thone, M. N., & Kwon, Y. J. (2020). Extracellular blebs: Artificially-induced extracellular vesicles for facile production and clinical translation. *Methods (San Diego, Calif.)*, 177, 135–145.
- Upadhy, R., Madhu, L. N., Attaluri, S., Gitai, D. L. G., Pinson, M. R., Kodali, M., Shetty, G., Zanirati, G., Kumar, S., Shuai, B., Weintraub, S. T., & Shetty, A. K. (2020). Extracellular vesicles from human iPSC-derived neural stem cells: MiRNA and protein signatures, and anti-inflammatory and neurogenic properties. *Journal of Extracellular Vesicles*, 9(1), 1809064.
- Vallabhaneni, H., Shah, T., Shah, P., & Hursh, D. A. (2023). Suspension culture on microcarriers and as aggregates enables expansion and differentiation of pluripotent stem cells (PSCs). *Cytotherapy*, 25(9), 993–1005.
- Vichai, V., & Kirtikara, K. (2006). Sulforhodamine B colorimetric assay for cytotoxicity screening. *Nature Protocols*, 1(3), 1112–1116.
- Walgrave, H., Penning, A., Tosoni, G., Snoeck, S., Davie, K., Davis, E., Wolfs, L., Sierksma, A., Mars, M., Bu, T., Thrupp, N., Zhou, L., Moechars, D., Mancuso, R., Fiers, M., Howden, A. J. M., De Strooper, B., & Salta, E. (2023). microRNA-132 regulates gene expression programs involved in microglial homeostasis. *Science*, 26(6), 106829.
- Wang, Q., Xu, S., Wang, B., Qin, Y., Ji, Y., Yang, Q., Xu, Y., & Zhou, Z. (2023). Chemokine receptor 7 mediates miRNA-182 to regulate cerebral ischemia/reperfusion injury in rats. *CNS Neuroscience & Therapeutics*, 29(2), 712–726.
- Wang, Z. G., He, Z. Y., Liang, S., Yang, Q., Cheng, P., & Chen, A. M. (2020). Comprehensive proteomic analysis of exosomes derived from human bone marrow, adipose tissue, and umbilical cord mesenchymal stem cells. *Stem Cell Research & Therapy*, 11(1), 511.
- Xia, Y., Hu, G., Chen, Y., Yuan, J., Zhang, J., Wang, S., Li, Q., Wang, Y., & Deng, Z. (2021). Embryonic stem cell derived small extracellular vesicles modulate regulatory T cells to protect against ischemic stroke. *ACS Nano*, 15(4), 7370–7385.

- Xia, Y., Ling, X., Hu, G., Zhu, Q., Zhang, J., Li, Q., Zhao, B., Wang, Y., & Deng, Z. (2020). Small extracellular vesicles secreted by human iPSC-derived MSC enhance angiogenesis through inhibiting STAT3-dependent autophagy in ischemic stroke. *Stem Cell Research & Therapy*, *11*(1), 313.
- Yu, L., Sui, B., Zhang, X., Liu, J., Hao, X., & Zheng, L. (2023). miR-92a-1-5p enriched prostate cancer extracellular vesicles regulate osteoclast function via MAPK1 and FoxO1. *Journal of Experimental & Clinical Cancer Research*, *42*(1), 109.
- Yuan, X., Chen, X., Zeng, C., Meckes, D. G., Jr., & Li, Y. (2022). Extracellular vesicle collection from human stem cells grown in suspension bioreactors. *Methods in Molecular Biology*, *2436*, 193–204.
- Yuan, X., Liu, Y., Bijonowski, B., Tsai, A. C., Fu, Q., Logan, T. M., Ma, T., & Li, Y. (2020). NAD<sup>+</sup>/NADH redox alterations reconfigure metabolism and rejuvenate senescent human mesenchymal stem cells in vitro. *Communications Biology*, *3*, 774.
- Yuan, X., Sun, L., Jeske, R., Nkosi, D., York, S., Liu, Y., Grant, S. C., Meckes, D. G. J., & Li, Y. (2022). Engineering extracellular vesicles by three-dimensional dynamic culture of human mesenchymal stem cells. *Journal of Extracellular Vesicles*, *11*(6), e12235.
- Zhang, L., He, S., Wang, Y., Zhu, X., Shao, W., Xu, Q., & Cui, Z. (2020). miRNA-20a suppressed lipopolysaccharide-induced HK-2 cells injury via NFκB and ERK1/2 signaling by targeting CXCL12. *Molecular Immunology*, *118*, 117–123.
- Zhang, X., Zhang, H., Gu, J., Zhang, J., Shi, H., Qian, H., Wang, D., Xu, W., Pan, J., & Santos, H. A. (2021). Engineered extracellular vesicles for cancer therapy. *Advanced Materials*, *33*(14), e2005709.
- Zhang, Z. G., Buller, B., & Chopp, M. (2019). Exosomes—beyond stem cells for restorative therapy in stroke and neurological injury. *Nature Reviews Neurology*, *15*(4), 193–203.
- Zhou, J., Flores-Bellver, M., Pan, J., Benito-Martin, A., Shi, C., Onwumere, O., Mighty, J., Qian, J., Zhong, X., Hogue, T., Amponsah-Antwi, B., Einbond, L., Gharbaran, R., Wu, H., Chen, B. J., Zheng, Z., Tchaikovskaya, T., Zhang, X., Peinado, H., ... Redenti, S. (2021). Human retinal organoids release extracellular vesicles that regulate gene expression in target human retinal progenitor cells. *Scientific Reports*, *11*(1), 21128.

## SUPPORTING INFORMATION

Additional supporting information can be found online in the Supporting Information section at the end of this article.

**How to cite this article:** Muok, L., Sun, L., Esmonde, C., Worden, H., Vied, C., Duke, L., Ma, S., Zeng, O., Driscoll, T., Jung, S., & Li, Y. (2024). Extracellular Vesicle Biogenesis of Three-dimensional Human Pluripotent Stem Cells in a Novel Vertical-Wheel Bioreactor. *Journal of Extracellular Biology*, *3*, e133. <https://doi.org/10.1002/jex2.133>